Smart Structures and Systems, *Vol. 23, No. 6 (2019) 589-613*
DOI: https://doi.org/10.12989/sss.2019.23.6.589

Experimental evaluation of an inertial mass damper and its analytical model for cable vibration mitigation

Lei Lu[1], Gaston A. Fermandois[2], Xilin Lu*[1],
Billie F. Spencer, Jr.[2], Yuan-Feng Duan[3] and Ying Zhou[1]

[1]State Key Laboratory of Disaster Reduction in Civil Engineering, Tongji University, Shanghai, 200092, China
[2]Department of Civil & Environmental Engineering, University of Illinois at Urbana-Champaign, IL, 61801, USA
[3]College of Civil Engineering and Architecture, Zhejiang University, Hangzhou 310058, China

(Received October 18, 2016, Revised February 20, 2018, Accepted February 24, 2018)

Abstract. Cables are prone to vibration due to their low inherent damping characteristics. Recently, negative stiffness dampers have gained attentions, because of their promising energy dissipation ability. The viscous inertial mass damper (termed as VIMD hereinafter) can be viewed as one realization of the inerter. It is formed by paralleling an inertial mass part with a common energy dissipation element (e.g., viscous element) and able to provide pseudo-negative stiffness properties to flexible systems such as cables. A previous study examined the potential of IMD to enhance the damping of stay cables. Because there are already models for common energy dissipation elements, the key to establish a general model for IMD is to propose an analytical model of the rotary mass component. In this paper, the characteristics of the rotary mass and the proposed analytical model have been evaluated by the numerical and experimental tests. First, a series of harmonic tests are conducted to show the performance and properties of the IMD only having the rotary mass. Then, the mechanism of nonlinearities is analyzed, and an analytical model is introduced and validated by comparing with the experimental data. Finally, a real-time hybrid simulation test is conducted with a physical IMD specimen and cable numerical substructure under distributed sinusoidal excitation. The results show that the chosen model of the rotary mass part can provide better estimation on the damper's performance, and it is better to use it to form a general analytical model of IMD. On the other hand, the simplified damper model is accurate for the preliminary simulation of the cable responses.

Keywords: stay cable; inerter; inertial mass damper; performance test; nonlinearities; real-time hybrid simulation test

1. Introduction

Cables are critical members of a cable-stay bridge. Due to their large flexibility, the relatively small mass and the extremely low inherent damping ratio, typically in the order of 0.1% (Yamaguchi and Fujino 1998), cables are prone to be excited by direct loads from wind, a combination of wind and rain, or via motion of the supported structure (Watson and Stafford 1988). Because the cable vibrations are often dominated by the resonance phenomena, a significant mitigation can be achieved at selected frequencies by properly tuning a passive damper (Krenk and Høgsberg 2005). This idea, firstly proposed in the early 1980's (Carrie 1980, Kovacs 1982), has been demonstrated its efficiency with various kinds of dampers, such as viscous dampers (Pacheco *et al.* 1993, Xu and Yu 1998, Yu and Xu 1998, Tabatabai and Mehrabi 2000, Krenk and Nielsen 2002, Main and Jones 2002a, Main and Jones 2002b, Fujino and Hoang 2008, Zhou *et al.* 2014), friction dampers (Weber *et al.* 2010), tuned mass dampers (Gu *et al.* 1994, Cai *et al.* 2006, Wu and Cai 2006) and magnetorheological dampers (Chen *et al.* 2004, Duan *et al.* 2005, Wang *et al.* 2005, Duan *et al.* 2007, Or *et al.* 2008, Duan *et al.* 2019b, Duan *et al.* 2019c). All these dampers can provide optimal additional damping ratios (Tabatabai and Mehrabi 2000, Zhou *et al.* 2014) for the specified modes of a cable after carefully choosing the damper parameters.

Because the cable itself has a very small transverse stiffness, the positive stiffness introduced by a passive damper, will decrease the damper's displacement which is already limited by its closeness to the support, and impair the efficiency of the dampers (Duan *et al.* 2006, Chen *et al.* 2015a). To solve this problem, an innovative passive damper called the inertial mass damper (IMD) (Lu *et al.* 2017) or tuned inerter damper (Lazar *et al.* 2015, Lazar *et al.* 2016, Luo *et al.* 2016) has been investigated by many researchers as alternative devices. Due to its pseudo negative stiffness and large inertial mass effect, the achievable modal damping ratios provided by the IMD can be up to nearly an order of magnitude larger than that of the traditional linear viscous damper (Lu *et al.* 2017).

In fact, inerters can refer to a family of dampers which harness the amplified inertial mass effect generated through a certain mechanism, especially in the field of mechanical engineering or automotive engineering. An inerter can be designed as a liquid-based (Kawamata 1989, Wang *et al.* 2011, Swift *et al.* 2013) damper or a mechanical-based damper. The latter is more widely reported and can be

*Corresponding author, Professor
E-mail: lxlst@tongji.edu.cn

Copyright © 2019 Techno-Press, Ltd.

ISSN: 1738-1584 (Print), 1738-1991 (Online)

realized by either a ball screw-ball nut system (Ikago *et al.* 2012a, Watanabe *et al.* 2012, Nakamura *et al.* 2013, Nakamura *et al.* 2014) or a rack and pinion system (Smith 2002, Saitoh 2012, Lazar *et al.* 2014b, Makris and Kampas 2016). Other designs for the inerters (Lazar *et al.* 2014b) have been proposed, such as the mechanical snubber (Severud and Summers 1980, Kawaguchi *et al.* 1991, Kelly 1997), the inertial mass damper (IMD) (Ohtake *et al.* 2006, Nakamura *et al.* 2014), the gyro-mass damper (GMD) (Saitoh 2012), the rotational inertia damper (RID) (Hwang *et al.* 2007) and the rotational inertia mass damper (RIMD) (Okamoto *et al.* 2017). Despite differences in specific details, all these devices share the same basic working principle, i.e., transferring the linear motion of the damper's ends to the high-speed rotation of the rotary mass through a certain mechanical system in order to generate very large inertial mass effect.

On the other hand, the energy dissipating ability of the inerter is very limited and mainly caused by friction: therefore, researchers intend to connect damping elements with the inerter, such as viscous element (Saito *et al.* 2004, Hwang *et al.* 2007, Ikago *et al.* 2012a, Saitoh 2012, Lu *et al.* 2017), electromagnetic element (Nakamura *et al.* 2014, Gonzalez-Buelga *et al.* 2015, Hjgsberg and Krenk 2016, Wang *et al.* 2016, Høgsberg and Krenk 2017) or eddy-current element (Chen *et al.* 2015b, Wen *et al.* 2016).

To the author's knowledge, in the 1970s, the inerter is firstly used by Japanese scholars as a kind of mechanical snubber for the vibration control of the pipe line in a nuclear power plant, given its insensitivity to high temperature and radiation (Severud and Summers 1980, Kawaguchi *et al.* 1991, Kelly 1997). Afterwards, Smith (2002) completes the analogy between mechanical and electrical systems (Firestone 1933) by treating the inerter as an analogy to the ungrounded capacitor. Then by using this method, the advantages of inerter have been comprehensively investigated, especially in automotive engineering (Chen *et al.* 2009, Papageorgiou *et al.* 2009, Liu *et al.* 2015, Chen *et al.* 2016a, Chen *et al.* 2016b, Shen *et al.* 2016a, Shen *et al.* 2016b).

Applications of inerters in civil structures have also been widely investigated. As these devices have large inertial mass effect with small self-weight, one promising strategy is to connect a spring in series with the inerter and make it tunable. The tuned inertial mass damper (TIMD) (Nakamura *et al.* 2013), tuned viscous mass damper (TVMD) (Ikago *et al.* 2012a) and tuned inerter damper (TID) (Lazar *et al.* 2014b, Lazar *et al.* 2014a, Lazar *et al.* 2014c, Wen *et al.* 2016), can all be viewed as realizations of this idea, and it is fair to classify them together as the tuned inerter-based damper (TIBD) (Wen *et al.* 2016). By determining the optimal damper parameters according to the fixed-point theory, the efficiencies and advantages of TIBD have been verified in details (Ikago *et al.* 2012a, Ikago *et al.* 2012b, Lazar *et al.* 2014b, Lazar *et al.* 2014a, Lazar *et al.* 2015, Lazar *et al.* 2016, Zhang *et al.* 2016, Zhang *et al.* 2017). Another plausible idea of the usage of inerter is to connect it with a traditional TMD, called tuned mass-damper-inerter (TMDI) (Marian and Giaralis 2013, Marian and Giaralis 2014, Giaralis and Marian 2016, Giaralis and Petrini 2017, Pietrosanti *et al.* 2017). This idea could efficiently reduce the actual mass needed from the traditional TMD and diminish the concern that the TIBD may not be excited sufficiently during the external excitation, especially when it is installed between stories. Meanwhile, the inerter has proved to be a good candidate as the energy dissipation devices in structures with base isolation (Saitoh 2012) and the stay-cable with an attached damper (Lazar *et al.* 2015, Lazar *et al.* 2016, Luo *et al.* 2016, Lu *et al.* 2017).

Usually, the damper force of the inerter is simplified as the product of an equivalent inertial mass and the relative acceleration of the damper's ends, which means the damper force should be linearly related to the damper displacement. However, testing results of inerters with different scales reveal that: the damper force-displacement curve has clear nonlinearities, and damper force results contain high-frequency components. There is still no unanimous conclusion for this phenomenon. The possible reasons might be associated to friction (Wang *et al.* 2011, Nakamura *et al.* 2014, Hessabi and Mercan 2016, Gonzalez-Buelga *et al.* 2017), backlash (Nakamura *et al.* 1988), internal stiffness (Wang and Su 2008a), loading method (Papageorgiou and Smith 2005, Papageorgiou *et al.* 2009) or some combinations of above factors (Wang and Su 2008a; Wang and Su 2008b, Sun *et al.* 2016). On the other hand, it is reported that the nonlinearities of inerters might only have little influences on the performances of GMD on the vehicle suspensions (Wang and Su 2008a) or optimal configured TIBD (Gonzalez-Buelga *et al.* 2017). But there are still no investigations about the influences of these nonlinearities on the performance of cable-IMD systems.

In this paper, the inerter with a "ball screw/ball nut" system, designated as IMD for short, is chosen to be investigated, because it is commonly proposed to be used in civil structures. Characteristics of the IMD are illustrated by numerical analysis and experimental tests. Two small-scale mechanical snubbers are selected, because they can be viewed as typical IMDs having only the rotary mass. The performance tests of the dampers are conducted under a series of harmonic excitations, and fundamental properties of the damper performance are demonstrated. Then, the mechanism of nonlinearities in the damper force is discussed in details, and an analytical damper model with variant stiffness is formed and validated with experimental results. Finally, the accuracy of the developed damper model is further evaluated by a real-time hybrid simulation test. Also, the effects of damper nonlinear responses over the performance of the cable-IMD system are assessed.

2. Description of a typical viscous IMD

A typical schematic of viscous IMD (VIMD) is shown in Fig. 1, which is based on the same concepts of the inertial mass damper proposed by Ikago *et al.* (2012a) and Nakamura *et al.* (2014). The VIMD consists of an inertial mass part and a viscous damping part. The inertial mass part is composed by a "ball screw" and a "ball nut" connected with a mass tube (flywheel). The viscous

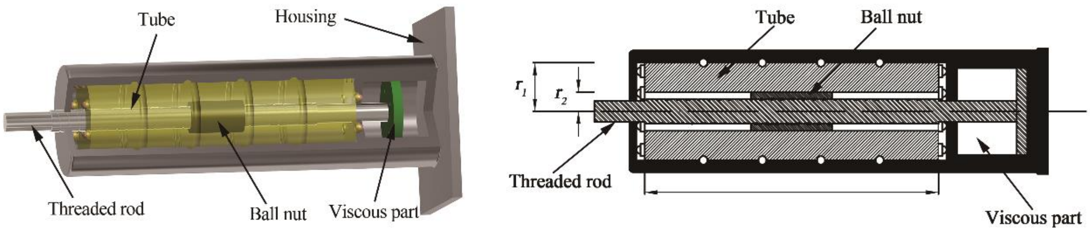

Fig. 1 Schematic of the VIMD

Fig. 2 IMD test specimens: (top) type I, (bottom) type II

damping part consists in three components: (i) a piston rod connected to a ball screw; (ii) a piston head (valve); and (iii) viscous fluid material. These components are covered by the same housing for modularity purposes.

Therefore, the common simplified damper forces $\overline{F_\mathrm{d}}$ expression is

$$\overline{F_\mathrm{d}} = \overline{m_\mathrm{e}}\ddot{u}_\mathrm{r} + \overline{c_\mathrm{d}}\dot{u}_\mathrm{r} + \overline{F_\mathrm{r}}\mathrm{sign}\left(\dot{u}\right) \tag{1}$$

where $\overline{m_\mathrm{e}}$ stands for the inertial mass generated by rotation, $\overline{c_\mathrm{d}}$ stands for the viscous damping coefficient provided by the damping component, u_r represents the relative displacement between two ends of the damper and $\overline{F_\mathrm{r}}$ stands for the damper friction.

In the VIMD, the inertial mass $\overline{m_\mathrm{e}}$ can be estimated by the following equation

$$\overline{m_e} = 2\left(\frac{\pi}{L_d}\right)^2 \left(r_1^2 + r_2^2\right)\rho_s \pi h_1 \left(r_2^2 - r_1^2\right) = n_m \cdot \overline{m_0} \tag{2}$$

where L_d represents the lead of ball screw; ρ_s is the density of the tube; r_1 and r_2 are respectively the inner and outer radius of the tube; h_1 is the length of the tube; $\overline{m_0}=\rho_\mathrm{s}\pi h_1\left(r_2^2\text{-}r_1^2\right)$ is the actual mass of the tube; and $n_\mathrm{m}=2(\pi/L_\mathrm{d})^2\left(r_2^2+r_1^2\right)$ is the magnification factor. It is reported that, the inertial mass $\overline{m_\mathrm{e}}$ could reach about 32 tons when the outer radius of the tube r_2 is just about 80 mm, and the related mass amplification factor n_m can practically achieve around 5000 or more (Lu *et al.* 2017).

3. Harmonic tests and results analysis

Previous studies are primarily based on the simplified damper model as presented in Eq. (1). In order to further investigate the characteristics of different IMDs, a more detailed analytical model is required. Because there are already many mature models for other energy dissipating components, the key to establishing a universal analytical model of the IMD is to find a proper representation of the inertial mass part. In this section, damper performance tests of two mechanical snubbers are conducted, and the related analytical model is proposed after carefully analyzing the experimental data.

3.1 Damper description and test setup

Two mechanical snubbers (Type SMS-B), provided by Sanwa Tekki Corporation are studied in this paper, as shown in Fig. 2. The specifications for the specimens are given in Table 1. The snubbers are mainly composed of a ball screw-ball nut system and a tube-like rotary mass, without any additional energy dissipation element. So they can be viewed as typical IMDs having only the rotary mass, which makes them perfect specimens to study the performances of rotary mass through a set of harmonic tests.

The loading assembly considered for this harmonic test is a MTS 204.63 servo-hydraulic actuator system, located at the Newmark Civil Engineering Laboratory from University of Illinois, Urbana-Champaign (USA), as shown in Fig. 4.

Table 1 Damper specifications

Damper Type	Stroke (mm)	Lead (mm)	Load range (kN)	Labeled inertial mass (kg)
Type I	±80	4	1.5	1500
Type II	±50	4	1.5	1500

Table 2 Maximum loading amplitudes (mm)

Frequency (Hz)	0.1	0.2	0.3	0.4	0.6	0.8	1	2	3	4	13
Type I	30	20	10	10	10	10	5	2	1	0.7	-
Type II	40	20	50	15	20	15	15	3	1	1	0.3

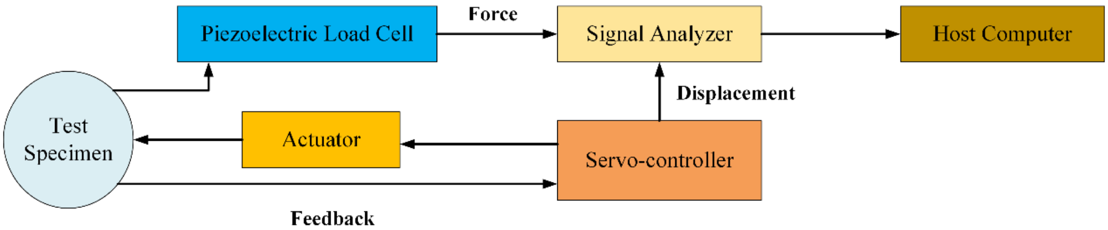

Fig. 3 Schematic plot of damper performance test

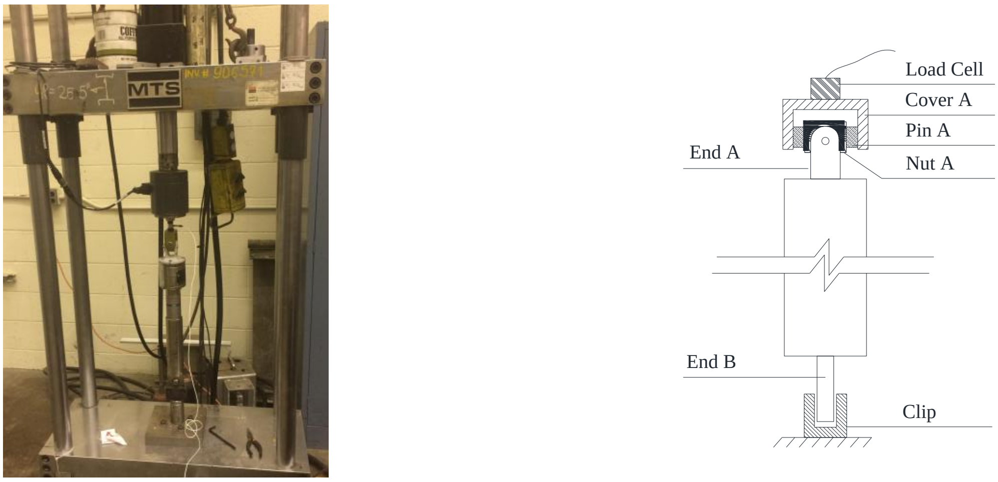

(a) Loading assembly (b) Connection details

Fig. 4 Loading assembly and connection details of the specimen

The dynamic actuator has a maximum load capacity of 100 kN (22 kips), with a maximum stroke capacity of ±75.2 mm (±3 in), and a servo valve with a rated flow of 15 gpm (gallons per minute), working at 3,000 psi of pump pressure. This loading assembly is adequate to conduct both harmonic tests and real-time hybrid simulation tests, as it will be explained in the following sections. For data acquisition purposes, a Vibpilot signal analyzer is included in the test setup, as shown in Fig. 3. The sampling rate for the harmonic tests is 2048 Hz.

According to the limitations of the damper and loading assembly, the load protocols are carefully selected to cover the interested frequency range (0.1 Hz to 15 Hz). The loading amplitude at each frequency is gradually increased. Maximum load amplitudes at the typical frequencies are shown in Table 2. The tapered load function embedded in the MTS control platform is used in order to reduce the pulse effect caused by the discontinuity of acceleration at the beginning and the end of each load case to protect the damper from overload (when the damper force is larger than its limitations). However, this function doesn't work well until the loading frequency is higher than 0.3 Hz. Therefore, the maximum amplitude of 0.2 Hz is smaller than those of 0.1 Hz and 0.3 Hz, and selected for safety purposes.

3.2 Test results and analysis

Fig. 5 shows time history plots of damper responses. As the responses of the two specimens are very similar to each other, only typical results of type II are shown here. To eliminate the noise effect, the experimental data have all been post-processed by a zero-phase low-pass filter, with its cut off frequency as 20 Hz, which is out of the main frequency ranges of damper responses.

Meanwhile, as shown in Figs. 5(d)-5(j), the damper force responses have significant high frequency components when the damper acceleration and displacement reach their local extremum. It is inconsistent with the simplified damper model, in which the damper force response should

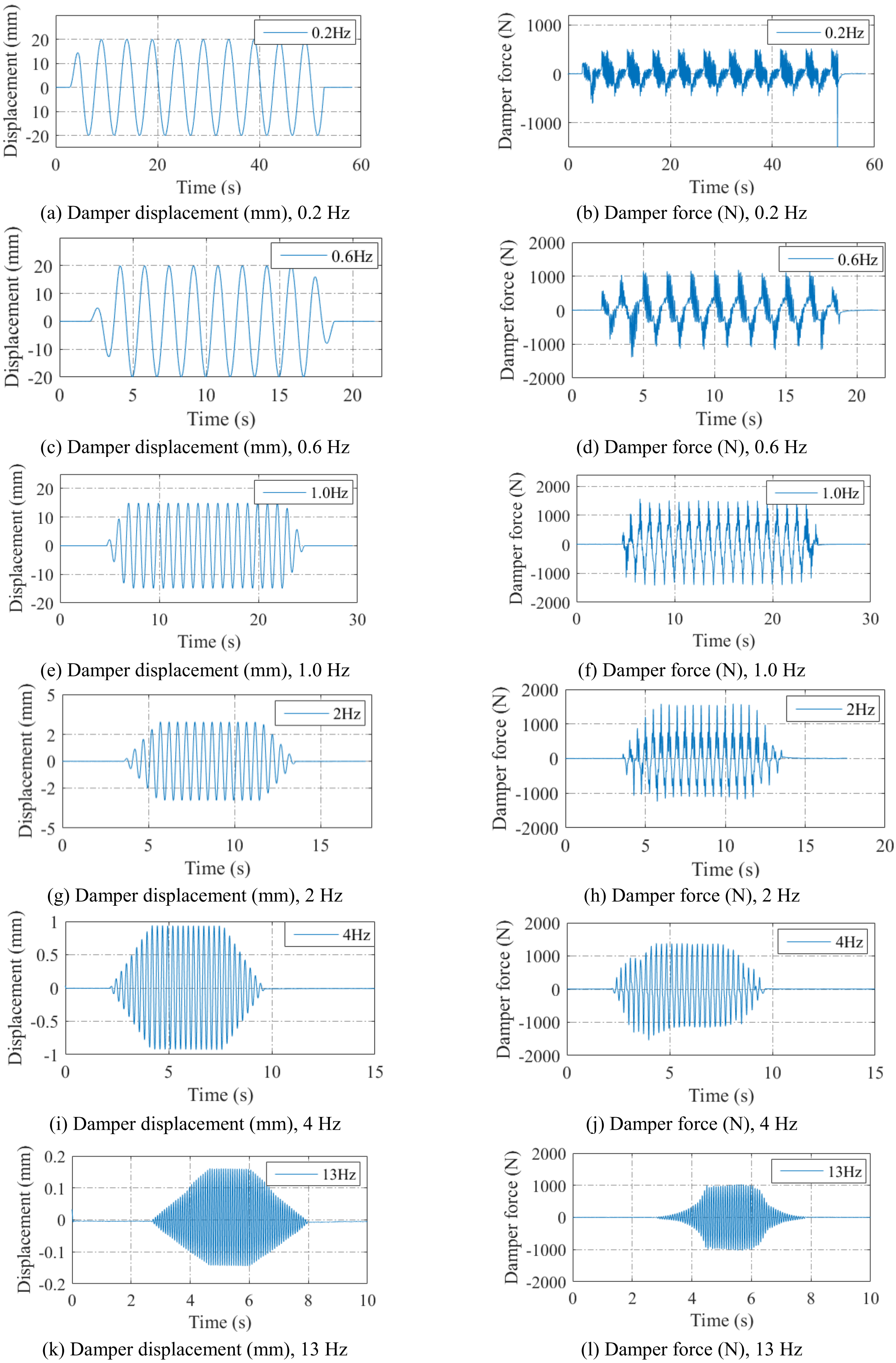

Fig. 5 Typical time history results of Type II damper in harmonic tests

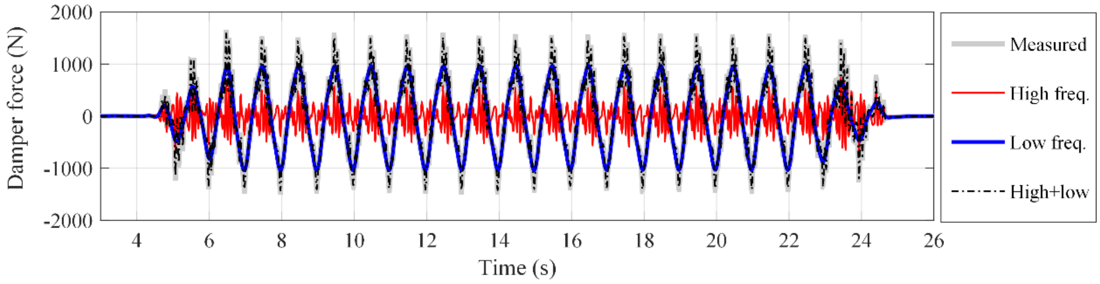

(a) Damper force responses (1 Hz)

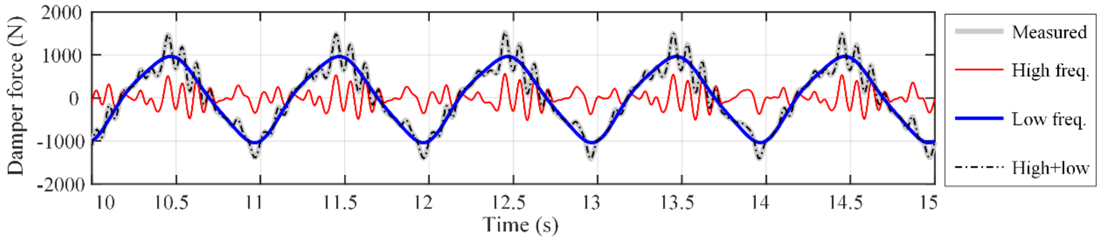

(b) Close-up view of damper force responses (1 Hz)

Fig. 6 Different frequencies components of damper force responses (1 Hz)

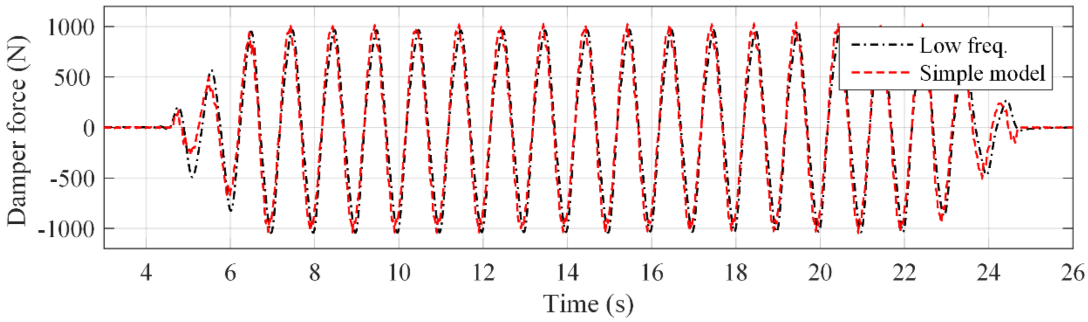

Fig. 7 Comparison between low frequency component results and simplified model (1 Hz)

be a smooth sinusoidal curve. The result at 1 Hz is shown in Fig. 6, where “Measured” stands for the measured data from the experiment, “High freq.” represents the result of the damper force filtered by a high-pass filter whose cut-off frequency is 3 Hz, “Low freq.” is the result of the damper force filtered by a low-pass filter whose cut-off frequency is 3 Hz, and “High+low” stands for the result which is the summation of the low and high frequency components. The result of the “High+low” case matches well with the measured data, and it is obvious that the high frequency component can’t be ignored when analyzing the damper force responses.

By comparing the data of the low frequency component and the results of the simplified model, as shown in Fig. 7, it can be observed that the simplified damper model is able to capture the low frequency component of the damper force, but not the high frequency component. Fig. 8 shows the power spectrum density (PSD) results of the measured damper force and the PSD of the same damper force filtered by the high-pass filter. It can be found that the range of the high frequencies is around 10~13 Hz, while there is a nonlinear increase of damper force for13 Hz as shown in Fig. 5(l), mainly associated to the resonance phenomenon. Therefore, it is safe to conclude that the high frequency components is connected with the damper self-vibration. As shown in the damper force responses of Figs. 5 and 6, this self-vibration happens when the damper acceleration and displacement reach their local extremum; a fluctuation of damper force can be observed which leads to an oscillation; therefore, the amplitude of the vibration is relatively larger when the damper is compressed and is relatively smaller when the damper is stretched.

Fig. 9 shows typical damper hysteretic loops corresponding to the time history results in Fig. 5. A negative stiffness and nonlinearities can be observed in the Figs. 9(a)-9(e), and the nonlinearities are more obvious in the upper part of the hysteretic loops. As the range of the damper’s natural frequency is relatively fixed, the hysteretic loop becomes smoother with the increase of the load frequency. Fig. 10 shows the typical hysteretic loops related to maximum load amplitudes with different frequencies. Because the damper force is mainly contributed by the

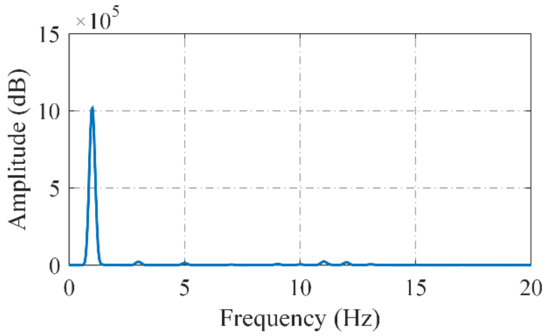

(a) PSD of the measured force

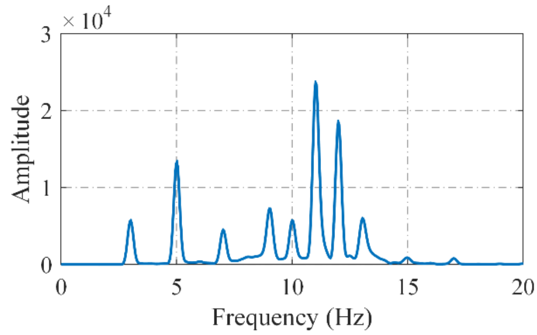

(b) PSD of the high-frequency components

Fig. 8 PSD of measured force and high-frequency components (1Hz)

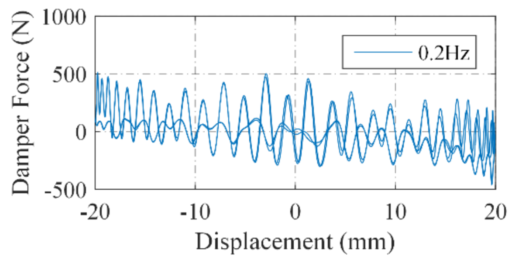

(a) Damper force-displacement plot, 0.2 Hz

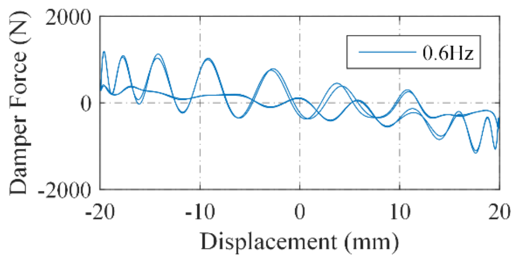

(b) Damper force-displacement plot, 0.6 Hz

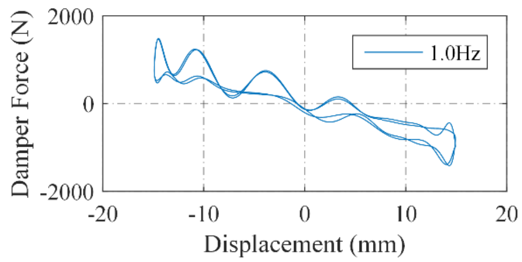

(c) Damper force-displacement plot, 1.0 Hz

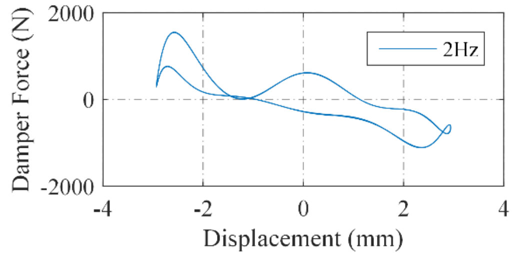

(d) Damper force-displacement plot, 2 Hz

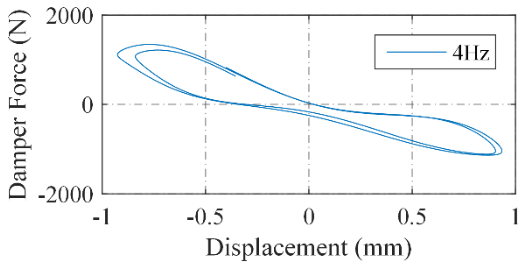

(e) Damper force-displacement plot, 4 Hz

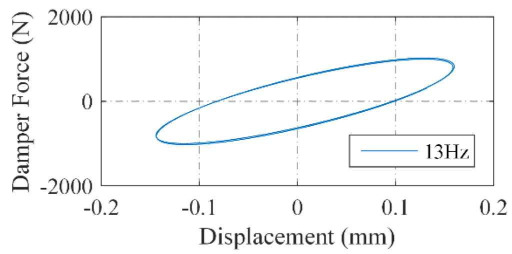

(f) Damper force-displacement plot, 13 Hz

Fig. 9 Typical damper force-displacement plots, damper Type II

equivalent inertial mass, the damper stiffness becomes smaller with the increase of the load frequency. Meanwhile, the maximum allowable displacement decreases, due to the damper force limitation. Also, because there is no energy dissipation element in the tested damper, the resulting hysteretic loops are very small and narrow.

Also, when the load frequency is close to the damper's natural frequency as shown in Fig. 9(f), an elliptical hysteretic loop with positive stiffness can be observed, which is associated with the damper's resonance. As a consequence, the inertial mass damper can also serve as a perfect dynamic spring under high frequency excitation (Severud and Summers 1980, Kawaguchi *et al.* 1991). However, in the field of cable vibration control, low frequency components make main contributions to the cable responses. Therefore, the research and discussion in the following sections will be focused on the results with the frequencies lower than 4 Hz.

As the nonlinearities are closely related to the damper's self-vibration, it is also important to discuss how the

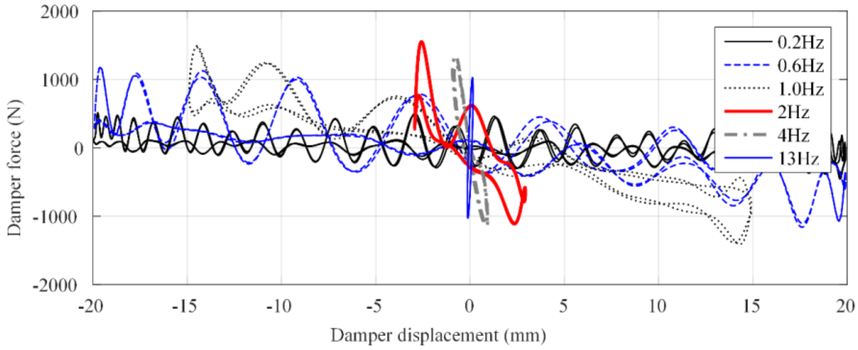

Fig. 10 Hysteretic loops under different loading frequencies

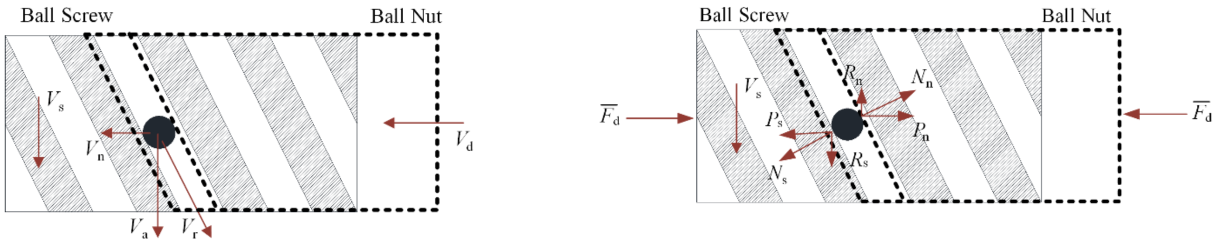

(a) Velocity diagram (b) Force diagram

Fig. 11 Damper analytical diagram (Damper is stretching out and moving toward neutral position)

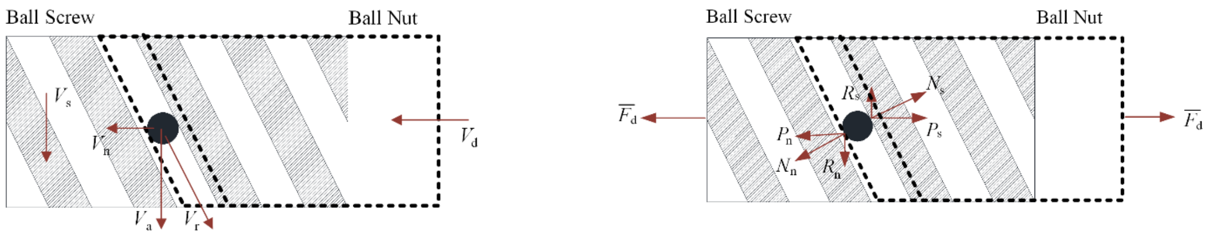

(a) Velocity diagram (b) Force diagram

Fig. 12 Damper analytical diagram (Damper is compressed and moving away from neutral position)

vibration can be excited. As mentioned in the previous section, the possible explanations may relate to the backlash within the damper-actuator system, the internal friction, and the loading method. Usually, when a gap is closed, a pulse may be introduced and results in a vibration. For the IMD, the gap within the damper-actuator system will close when the direction of the acceleration/load changes at the neutral position (as shown in Figs. 11 and 12), and the damper force will almost remain the same during this process. However, because the damper force is mainly contributed by the inertial mass effect, as the acceleration is very small at that point, the damper force should be very small too. Similarly, the direction of the friction does change at the peaks of the damper displacement, but the value of friction is also relatively small (Nakamura *et al.* 2014) compared to the large damper force. Therefore, the gap and the internal friction are not the main reasons for the nonlinearities of the damper force.

On the other hand, because the load process is displacement-controlled, the input displacement curve is relatively smooth, while the input acceleration curve is not smooth especially at those peak points, as shown in Fig. 13. Because the response of the IMD damper is related to the acceleration, a fluctuation in acceleration will lead to a fluctuation in the damper force, which will result in the self-vibration of the damper. Further, as shown in Fig. 14, the measured damper force cannot be estimated accurately by the simplified model even using the input acceleration. But the places where the fluctuations happen in both results, are close to each other. Therefore, it can be concluded that the nonlinearities in the damper forces during the sinusoidal tests are closely related to the internal stiffness of the IMD and excited by the unsmooth input acceleration due to the displacement-controlled load process. Note that, the input acceleration will not be smooth when the IMD is in the actual service, i.e., under seismic or wind load.

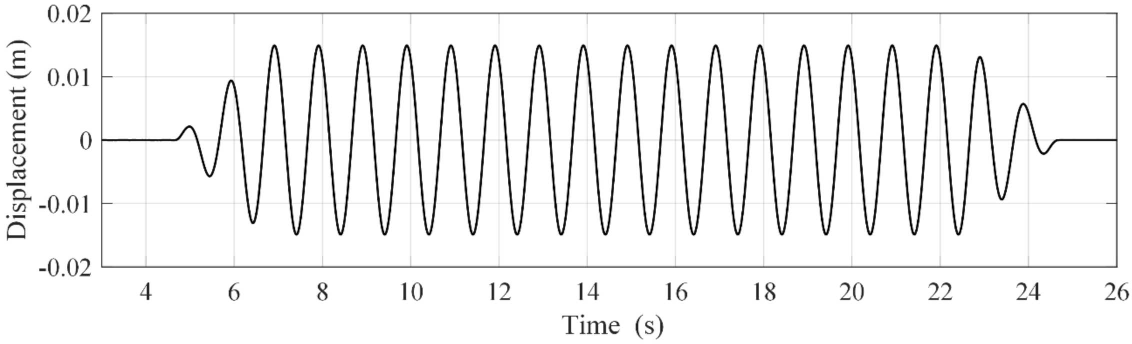

(a) Time history of the input displacement, 1 Hz

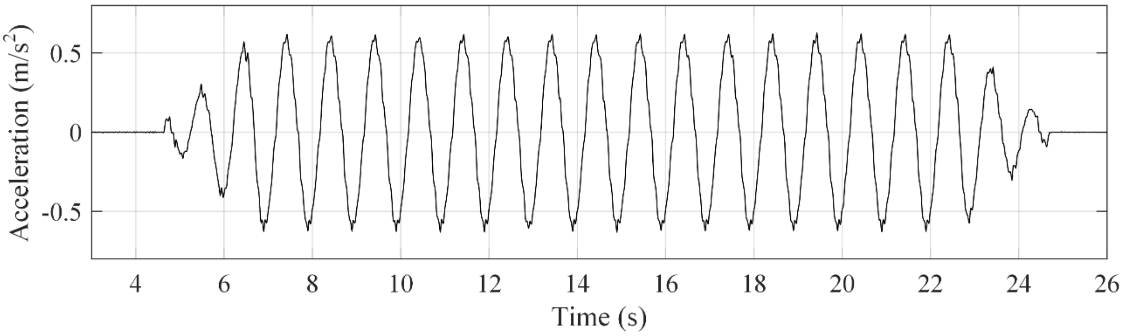

(b) Time history of the input acceleration, 1 Hz

Fig. 13 Comparison of the input displacement and the acceleration, 1 Hz

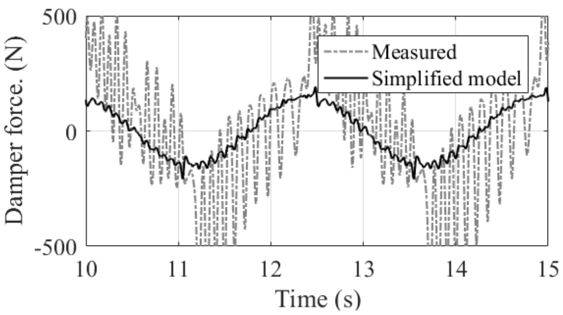

(a) 0.4 Hz

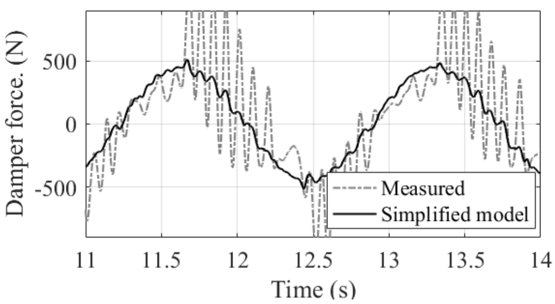

(b) 0.6 Hz

Fig. 14 Comparison between the measured force and the force derived by the simplified model

Therefore, it is important to consider the internal stiffness of the IMD when forming an analytical damper model for further researches.

4. Analytical model of the IMD and model verifications

4.1 Analytical model of the IMD with variant stiffness

Ideally the IMD can be represented by the following three main parts: rotary mass, ball screw and ball nut, as shown in Fig. 15, where u_d represents the relative displacement of the damper; θ_i and θ_d are the angular displacements of the rotary mass and ball screw, respectively; l_d as the lead of the ball screw; l_c is set as the distance between the middle point of the rotary mass and the middle point of the ball nut, and it is time-variant; l_r is the length of the rotary mass; l_f is the distance between the middle point of the rotary mass and the middle point of the bass screw, holding $l_c(t)= l_f+ u_d(t)$. Based on the force/displacement diagram, a detailed force analysis can be conducted, as shown in Fig. 16, where $\overline{k_e}$ is the equivalent stiffness of the damper, which can be safely assumed to be equal to the axial stiffness of the damper's components in this case; c_i is damping coefficient; J_i is the moment of inertial of the rotary mass; T_s represents the torque of the ball screw.

It can be viewed that $\overline{k_e}$ is contributed by the axial/rotational stiffness of the ball screw/ball nut system, and the axial stiffness of the axial bearing and housing system. The value of latter two are relatively large, so it is reasonable to assume that $\overline{k_e}$ is mainly contributed by the

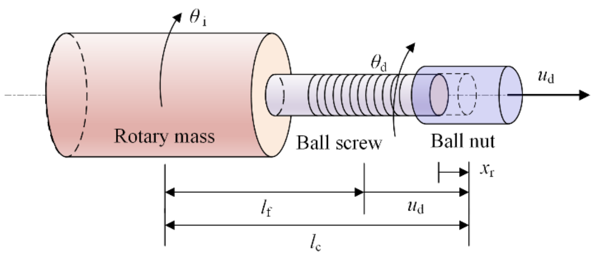

Fig. 15 Displacement diagram of the IMD

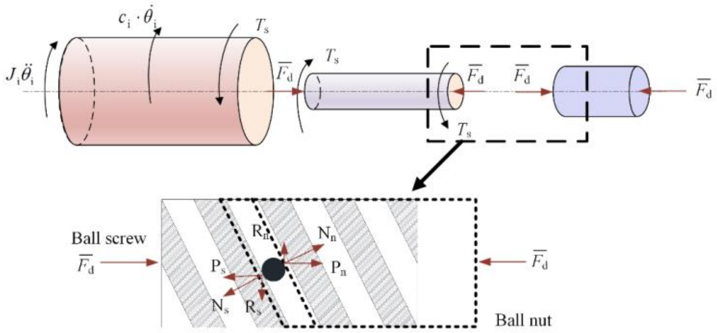

Fig. 16 Force diagram of the IMD

axial stiffness $\overline{k_s}$ and rotational stiffness $\overline{k_T}$ of the ball screw/ball nut system, as follows

$$\frac{1}{\overline{k_e}} = \frac{1}{k_s} + \frac{1}{k_T\left(2\pi/l_d\right)^2} \tag{3}$$

Substitute the equations of $k_s = A\mathrm{E}/l_c(t)$ and k_T=GJ_s//$l_c(t)$ into Eq. (3), where A, E, G and J_s are the section area, elasticity modulus, shear modulus and the moment of inertial of the ball screw respectively. Note that $l_c(t)= l_f+ u_d(t)$, therefore, $\overline{k_e}$ can be represented as a variant stiffness related to the damper displacement

$$\overline{k_e}\left(t\right)=k_0 \cdot \frac{l_f}{l_f + u_d\left(t\right)} \tag{4}$$

where

$$k_0 = \frac{\gamma_b A\mathrm{E}}{l_f\left[1+\gamma_b \dfrac{A\mathrm{E}}{\mathrm{G}J_s}\left(\dfrac{l_d}{2\pi}\right)^2\right]} \tag{5}$$

where γ_b is the compensation factor indicating the influence of the axial stiffness of the bearing/housing system on the k_s, which is set as 1 in this paper.

Then, the equation of motion of the damper can be formed as follows

$$J_i\ddot{\theta}_i + c_i\dot{\theta}_i = T_s \tag{6}$$

where

$$J_i = \frac{1}{2}m_r\left(r_i^2 + r_o^2\right),\ c_i=c\left(2\pi r_o\right)l_r r_o = 2c\pi l_r r_o^2 \tag{7}$$

where m_r is the mass of the rotary mass; r_i and r_o are the inner and outer radius of the rotary mass; r_s is the radium of the ball screw; c is the viscous coefficient. Set x_i is the horizontal displacement related to θ_i, following relationship can be formed

$$\theta_i = \frac{2\pi}{l_d}x_i \tag{8}$$

According to the force equilibrium of the ball screw

$$T_s = r_s R_s = r_s \overline{F_d}\tan\varphi \tag{9}$$

where φ is the lead angle of the ball screw, that satisfies

$$\tan\varphi = \frac{l_d}{2\pi r_s} \tag{10}$$

Also, the damper force $\overline{F_d}$ holds the following equation

$$\overline{F_d} = \overline{k_e}\left(u_d - x_i\right) \tag{11}$$

By substituting Eqs. (11) and (9) into Eq. (6), the analytical model of the IMD considering the self-stiffness of the damper can be established as follows

$$\begin{cases} \overline{F_d} = \overline{m_e}\ddot{x}_i + \overline{c_d}\dot{x}_i \\ \overline{m_e}\ddot{x}_i + \overline{c_d}\dot{x}_i + \overline{k_e}x_i = \overline{k_e}u_d \end{cases} \tag{12}$$

where $\overline{m_e}$ is the equivalent inertial mass of the damper, and $\overline{c_d}$ is the equivalent damping coefficient of the damper, holding

$$\overline{m_e} = J_i\left(2\pi/l_d\right)^2,\ \ \overline{c_d} = \left(2\pi/l_d\right)^2 c_i \tag{13}$$

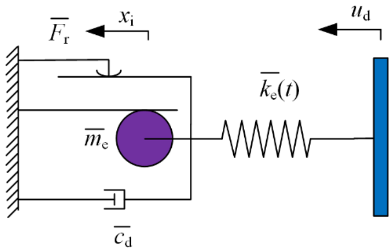

Fig. 17 Analytical model of the IMD

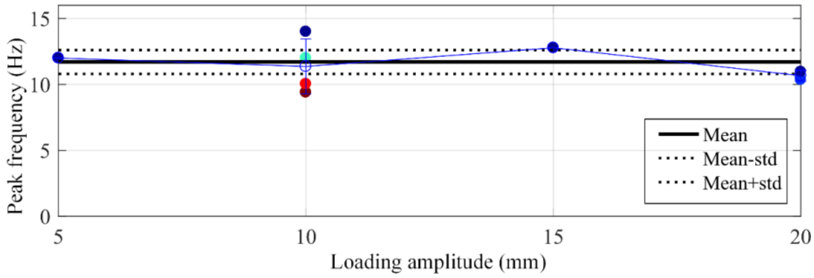

(a) Type I

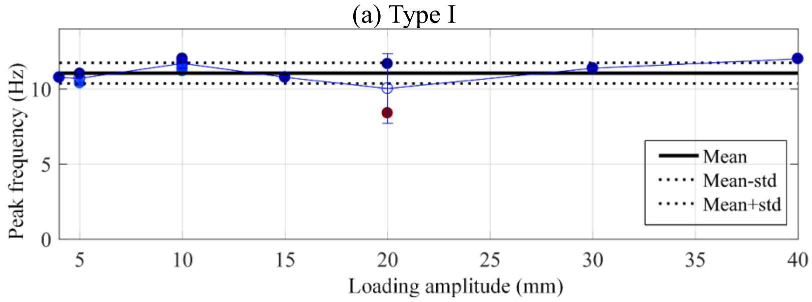

(b) Type II

Fig. 18 Peak frequencies of different load amplitudes

Note that, $(2\pi/l_d)^2$ is known as the amplifier factor. For the convenience of following discussions, equivalent natural frequency $\omega_e=\sqrt{k_0/\overline{m}_e}$ and equivalent damping ratio $\xi_e=\overline{c}_d/2\sqrt{k_0\overline{m}_e}$, are introduced.

The diagram of the analytical model of the IMD is shown in Fig. 17, where $\overline{F}_r$ is a possible friction force, which is usually small and can be neglected. Also, notice that this model can be a general damper model and used for other kinds of inertial mass damper using ball screw/ball nut system with different energy dissipating element. However, in those cases, the equations of $\overline{m}_e$, $\overline{k}_e$ and $\overline{c}_d$ might be different.

By introducing the relative displacement of the damper ends, $x_i=x_r+u_d$, substituting this expression into Eq. (12), and multiplying both sides of the equation by the amplifier factor, the following relationship is obtained

$$-\left(\overline{m}_e\ddot{x}_r+\overline{c}_d\dot{x}_r\right)-\overline{k}_e x_r=\overline{m}_e\ddot{u}_d+\overline{c}_d\dot{u}_d \tag{14}$$

It can be noticed that the right-hand-side of the equation is the damper force calculated by the simplified model, named as $\overline{F}_{d0}$, meanwhile, $-\overline{k}_e x_r$ equals to the damper force calculated by the analytical model, named as $\overline{F}_d$. Therefore, Eq. (14) can be formulated as

$$\overline{F}_d=\overline{F}_{d0}+\left(\overline{m}_e\ddot{x}_r+\overline{c}_d\dot{x}_r\right) \tag{15}$$

And the term between brackets on the right-hand-side of the above equation, represents the force fluctuation caused by the self-vibration of the damper.

4.2 Model validation

In this section, parameters of the analytical model are identified, based on the data of the tested dampers and other data gathered from the literature. Through this parameter identification procedure, the feasibility of the chosen analytical model is verified.

4.2.1 Parameter identifications for the tested damper

To identify the model parameters of the tested specimens, an optimization problem is formulated. Set the objective function J as the root mean square error (RMSE) between the measured and the calculated damper force.

$$J = \left[\frac{1}{N} \sum_{i}^{N} \left(F_{ci} - F_{ti} \right)^2 \right]^{\frac{1}{2}} \tag{16}$$

where F_{ci} and F_{ti} are the calculated and measured damper force at the time step i, respectively. Then, the problem is to find the optimal model parameters such that the objective function J is minimized. To solve this optimization problem, the pattern search method (Audet and Dennis Jr 2002) is used, and the numerical implementation is developed in Matlab/Simulink. The equivalent inertial mass $\overline{m_e}$ and the equivalent damping ratio ξ_e are chosen as parameters for identification. For this particular case, the friction is neglected, and the damping effect is approximated by the equivalent damping ratio ξ_e of the damper. The box constraints (i.e., lower and upper limits) for parameters $\overline{m_e}$ and ξ_e are chosen as [1000, 5000] and [0.001, 0.5], respectively.

The equivalent damper stiffness $\bar{k}_e$ is related to the damper displacement, so the high frequency components of the damper force distribute in a range, as it is shown in the case of 1Hz (Fig. 8). However, by calculating the peak frequencies of the high frequency components for different load amplitudes, it can be found that these frequencies vary slightly around their average value, as it is shown in Fig. 18. Note that only the cases of which loading amplitude is larger than l_d, are selected (0.1 Hz-1 Hz), in order to exclude the influences caused by the high-order modes of the ball screw. Therefore, it is reasonable to assume that the peak frequency is related to the damper's stiffness at the neutral position, and k_0 can be derived by using the average value of the peak frequencies.

The damper parameters are firstly identified for the typical experimental results of Type II when load amplitudes are the maximum reachable amplitudes at each frequency. The measured results and the simulated damper responses with these preliminarily identified damper parameters are shown and compared in Fig. 19. It indicates that the analytical model can properly simulate the behavior of the tested damper, showing negative stiffness and self-vibration characteristics. The errors between the measured and simulated results may be attributed to the assumption of the equivalent damping ratio. Because the tested damper doesn't have any energy dissipating element, and its mechanism of the energy dissipation is complicated and may come from friction and collision, which are hard to be estimated accurately by using the equivalent damping approach. Also, the simulated results show slower attenuations of the damper vibration than the experimental observations at the end of the loading process, especially for low frequency cases. One of the reasons for this effect might be that the actuator is involved in energy dissipation from the system at this stage because of the tapered load.

Then, the damper parameters identification is conducted for all the load cases of both Type I and Type II dampers, and the relationships of the identified damper parameters with the load frequencies and amplitudes are analyzed.Figs. 20 and 21 respectively show the results of identified $\overline{m_e}$ and ξ_e under different load frequency and amplitude; the color shade of each data point indicates the load amplitude at each frequency; meanwhile, the error bars indicate the mean value and the standard variation at each frequency; also, the black solid line shows the mean value of the identified parameters, by removing a maximum and a minimum point, and the black dash line shows the mean value $\pm$ one standard deviation of the identified parameters.

The identification results show that the equivalent inertial mass, $\overline{m_e}$, does not vary much for most load frequencies and amplitudes, except when the load frequency is 0.3 Hz and 0.4 Hz for Type I damper. Because the taped function of the loading system is malfunctioned at these cases, there is only one result for parameter identifications, which may introduce error. The fact that $\overline{m_e}$ is insensitive to the variant of load frequencies and amplitude, indicates it doesn't have a clear relationship with the load frequency and the amplitude, which is in agreement with the theoretical analysis from previous sections.

As stated previously, the energy dissipation of the tested specimens might be associated with factors related to the load frequency or amplitude, such as friction or collision. As shown in Figs. 21 and 22, the equivalent damping ratio ξ_e has a clear correlation with the load amplitude, but it is less obviously connected with the load frequency. Because, as shown in Table 2, when the load amplitudes are similar for the load cases of 0.3-0.8 Hz, the values of ξ_e are also close to each other. It indicates that the energy dissipation of the tested damper is mainly provided by friction. Then, a fitting process is conducted to find a relationship between ξ_e and the load amplitude, and the results are shown in Eq. (17).

$$\xi_e = \frac{c_1}{A_l + c_2} \tag{17}$$

where A_l stands for the load amplitude (mm); and c_k (k=1,2) are the fitting coefficients. Table 3 shows the common indices for the evaluation of the fitting results, indicating it is an acceptable fitting.

Note that, for the case when the load amplitude is very small (i.e., less than 0.1 mm), Eq. (17) will produce unrealistic large damping ratio. Also, the damping ratio is around 0.3 when the load amplitude is less than 0.1 mm, so it is reasonable to use a piecewise function for the equivalent damping ratio ξ_e, as shown in Eq. (20).

Therefore, the identified parameters of the tested dampers can be determined and summarized in Table 4, and four common indices in Table 3 are involved to evaluate the fitting results: SEE stands for the Sum of Squares due to Error; RMSE stands for the Root Mean Square Error; R-square stands for the coefficient of determination;

Table 3 Evaluation of the fitting results

Damper Type	SSE	R-square	Adjusted R-square	RMSE
SMS-B Type I	0.0269	0.8887	0.8847	0.03101
SMS-B Type II	0.0040	0.9609	0.9597	0.01112

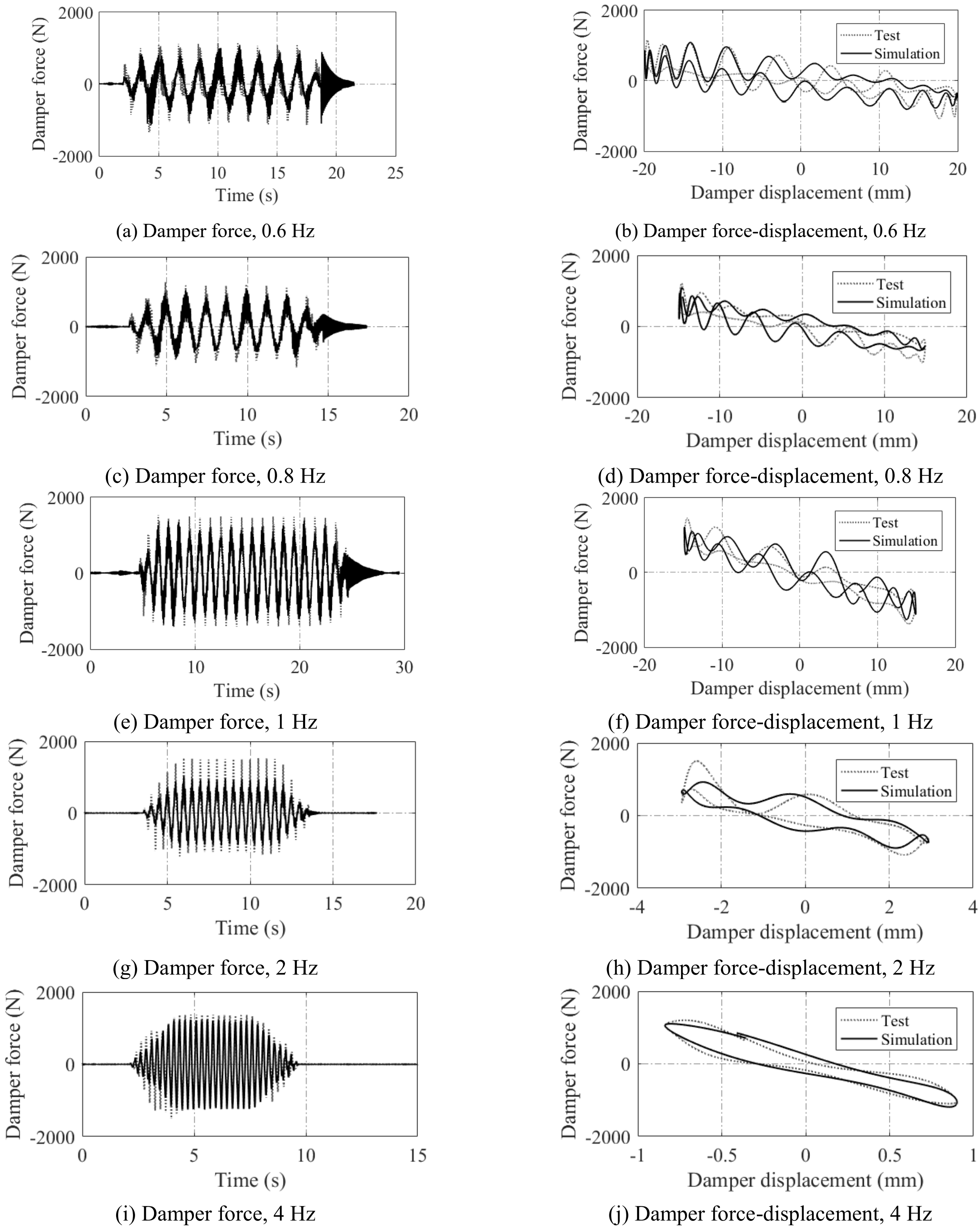

(a) Damper force, 0.6 Hz (b) Damper force-displacement, 0.6 Hz

(c) Damper force, 0.8 Hz (d) Damper force-displacement, 0.8 Hz

(e) Damper force, 1 Hz (f) Damper force-displacement, 1 Hz

(g) Damper force, 2 Hz (h) Damper force-displacement, 2 Hz

(i) Damper force, 4 Hz (j) Damper force-displacement, 4 Hz

Fig. 19 Comparison of damper responses with preliminarily identified model parameters

Table 4 Identified damper parameters of the tested IMD

Damper type	$\overline{m}_e$ (kg)	k_0 (N/m)	ξ_e	
			c_1	c_2
SMS-B Type I	1509	0.9×10^7	0.100	0.236
SMS-B Type II	1589	1.2×10^7	0.079	0.153

Adjusted R-square stands for the degree-of-freedom adjusted coefficient of determination. The first two indicate a good curve fitting when their values are close to 0; while the others indicate a good fitting when their values are close to 1.

It can be found that the two tested specimens have similar parameters, except the stiffness of Type I is slightly lower in accord with its longer stroke.

Table 5 Key experimental parameters of the EIMD (Nakamura *et al*. 2014)

Damper type	**Flywheel's equivalent mass** (kg)	**Terminal resistance** (Ω)	**Damping coefficient** (Ns/m)	**Load frequency** (Hz)	**Load amplitude** (mm)
Small-scale	6.00×10^{3}	0	1.15×10^{3}	1	6
Full-scale	2.00×10^{6}	0	3.05×10^{6}	0.5	10

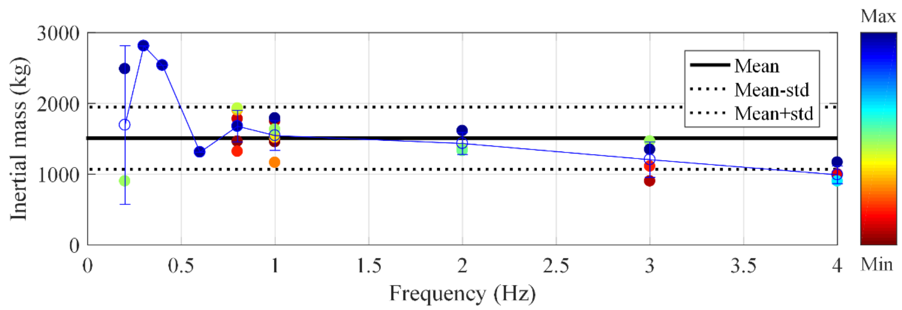

(a) Type I

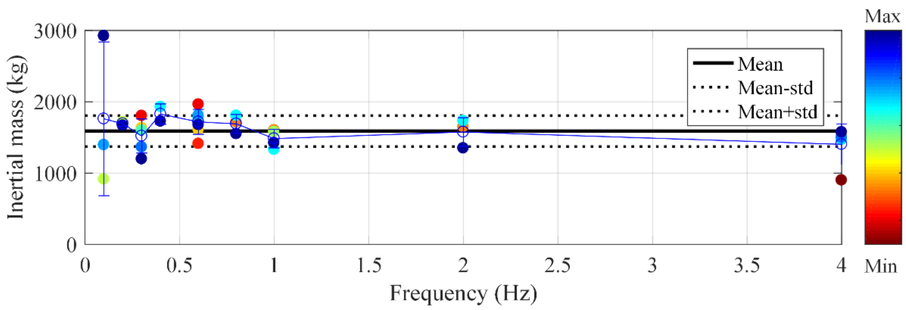

(b) Type II

Fig. 20 Identified $\overline{m_e}$ under different load frequencies and amplitudes

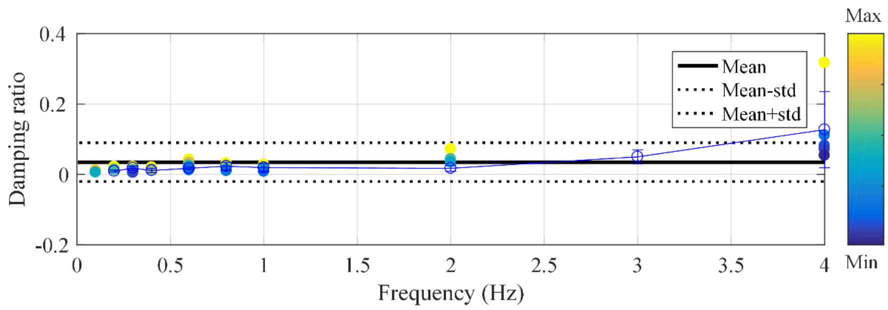

(a) Type I

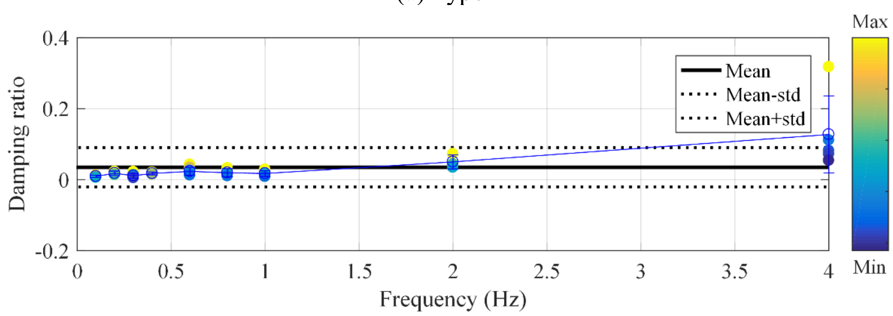

(b) Type II

Fig. 21 Identified ξ_e under different load frequencies and amplitudes

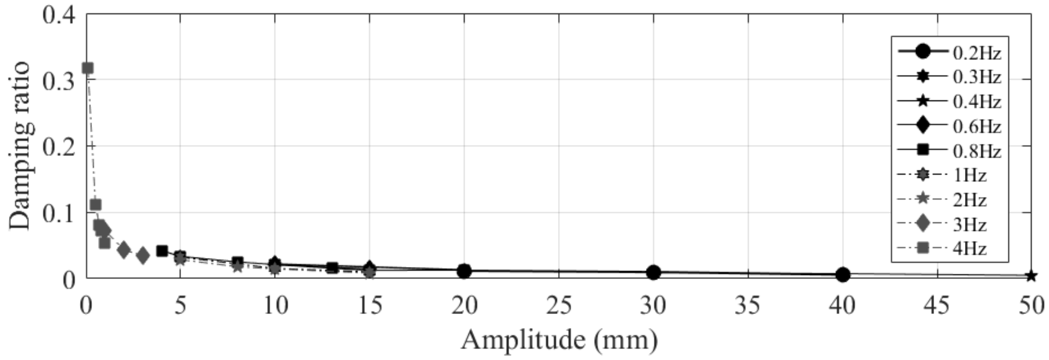

(a) Type I

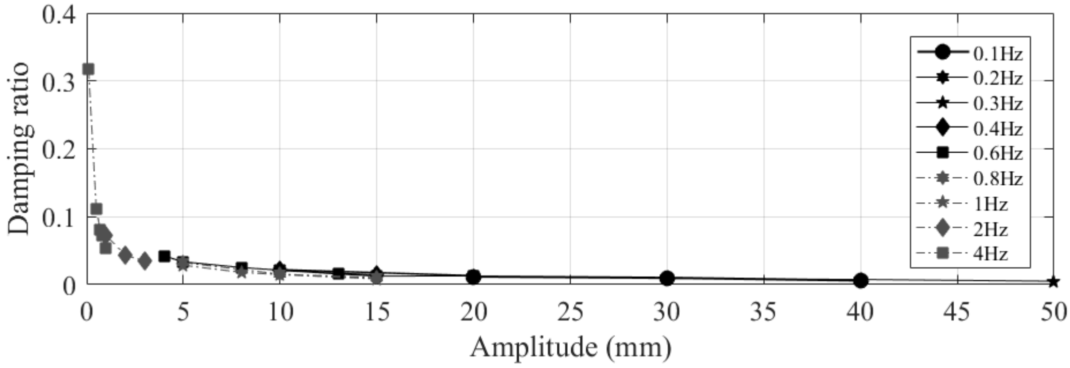

(b) Type II

Fig. 22 Relationship between ξ_e and displacement amplitude under different frequency

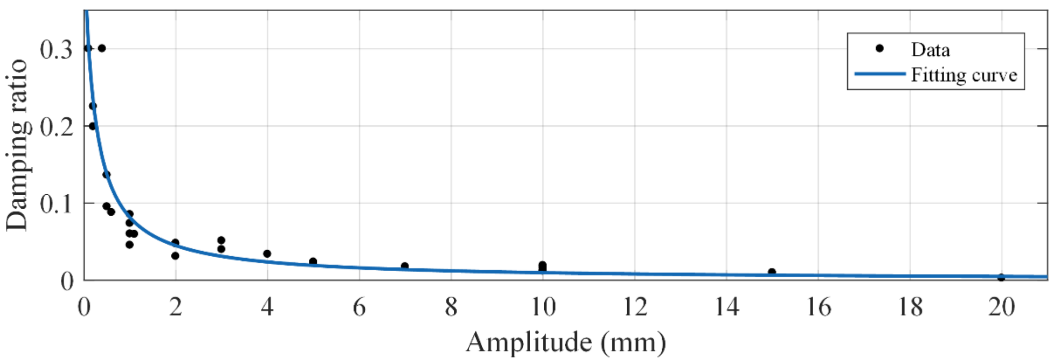

(a) Type I

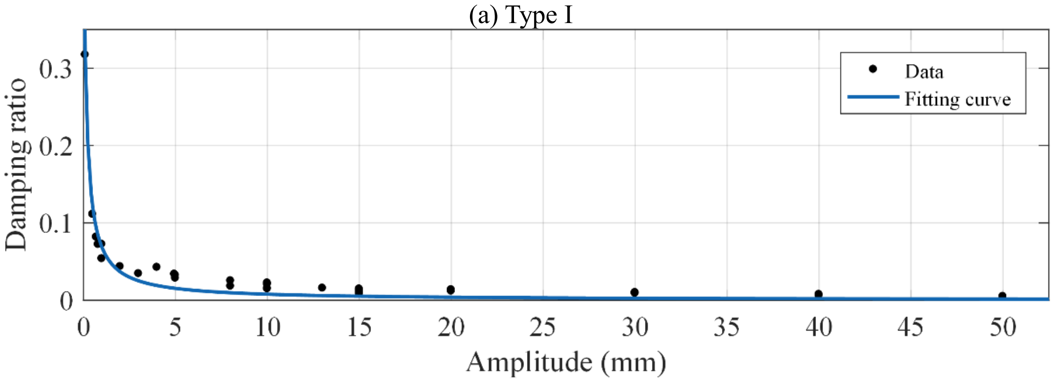

(b) Type II

Fig. 23 Fitting curve of ξ_e and displacement amplitude

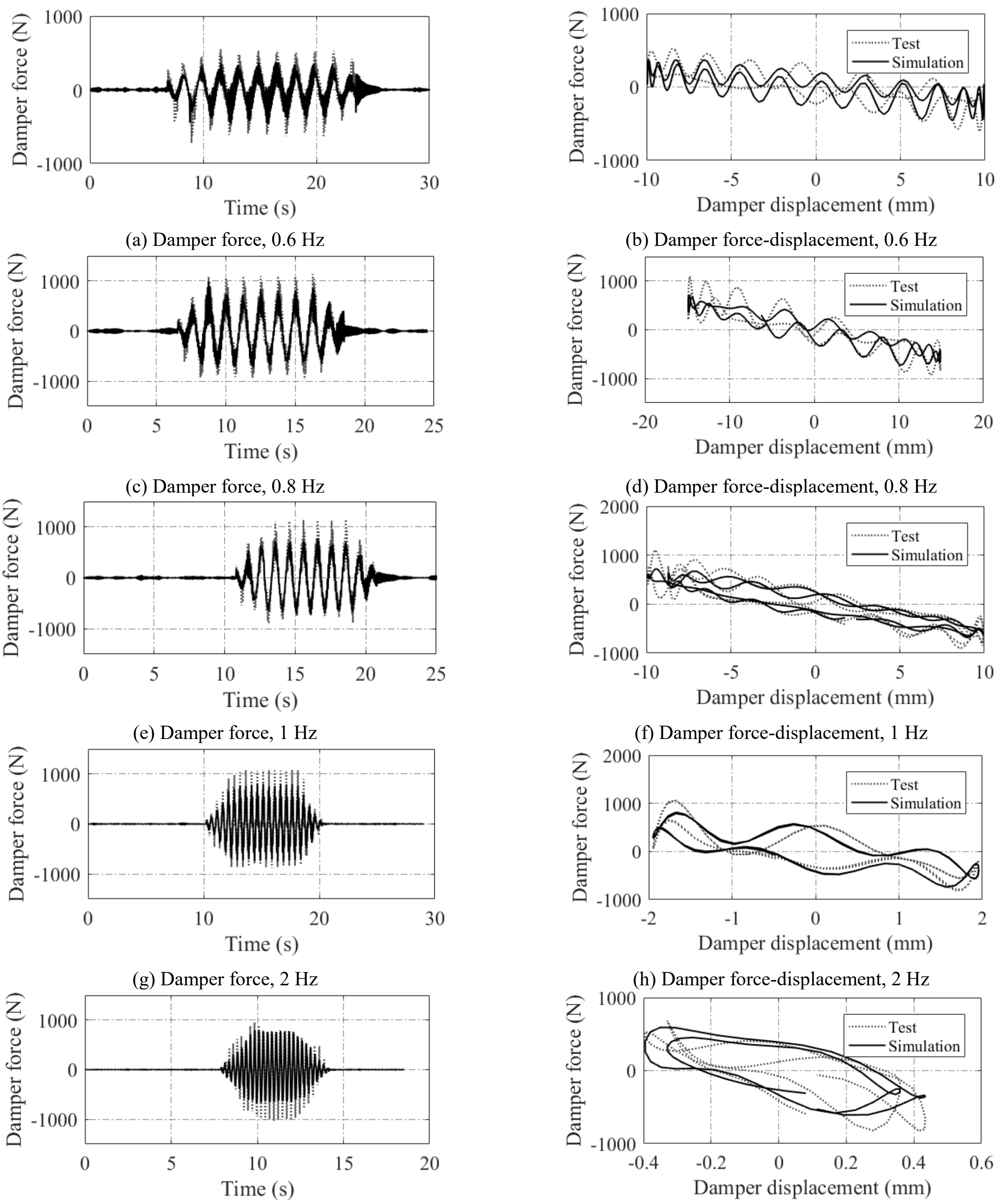

(a) Damper force, 0.6 Hz
(b) Damper force-displacement, 0.6 Hz
(c) Damper force, 0.8 Hz
(d) Damper force-displacement, 0.8 Hz
(e) Damper force, 1 Hz
(f) Damper force-displacement, 1 Hz
(g) Damper force, 2 Hz
(h) Damper force-displacement, 2 Hz
(i) Damper force, 4 Hz
(j) Damper force-displacement, 4 Hz

Fig. 24 Comparison of damper responses with identified model parameters, Type I

Meanwhile, comparisons between the measured and simulated damper forces are shown in Figs. 24 and 25. Note that the errors are slightly larger than those in Fig. 19 for Type II, but still acceptable.

$$\xi_e = \begin{cases} \dfrac{c_1}{A_1 + c_2} & A_1 > 0.1 \\ 0.3 & A_1 \le 0.1 \end{cases} \tag{18}$$

4.2.2 Parameter identifications for reported EIMDs

It is important to verify the capability of the proposed damper model in predicting the performances of other IMDs, especially the large-scale dampers with the energy dissipation element. Two typical experimental results of the electromagnetic inertial mass damper (EIMD) reported in the previous study (Nakamura *et al.* 2014) are simulated by the proposed analytical damper model and the ideal

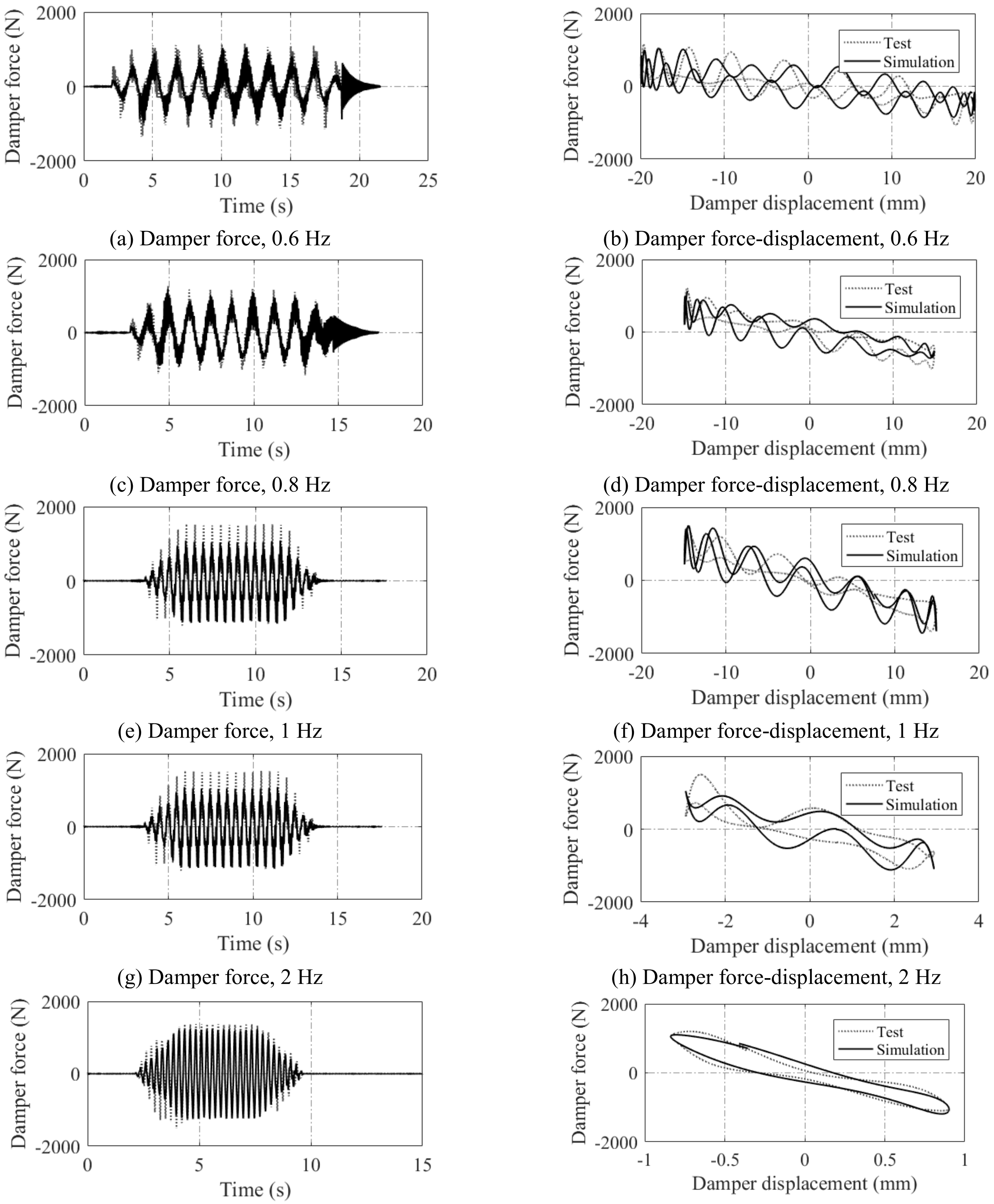

(a) Damper force, 0.6 Hz
(b) Damper force-displacement, 0.6 Hz
(c) Damper force, 0.8 Hz
(d) Damper force-displacement, 0.8 Hz
(e) Damper force, 1 Hz
(f) Damper force-displacement, 1 Hz
(g) Damper force, 2 Hz
(h) Damper force-displacement, 2 Hz
(i) Damper force, 4 Hz
(j) Damper force-displacement, 4 Hz

Fig. 1 Comparison of damper responses with identified model parameters, Type II

simplified model. The electromagnetic element is approximated by a viscous element, i.e., the dash-pot element ($\overline{c_{\mathrm{d}}}$) in the proposed damper model, and the unsmooth input acceleration is simulated by a backlash block in MATLAB. Key testing parameters of the EIMD are summarized in Table 5. Note that the small-scale/large-scale in the column of damper type are determined by the equivalent mass of the flywheel.

Through the parameter identification procedure mentioned previously, the optimal damper parameters of the EIMDs are obtained and are presented in Table 6, where h_{d} is the length of the backlash. Fig. 26 shows the comparison of the damper hysteretic plots of the testing results and simulation results. Note that, for the simplified model, the damper parameters are chosen from Table 5, which might not be their optimal parameters.

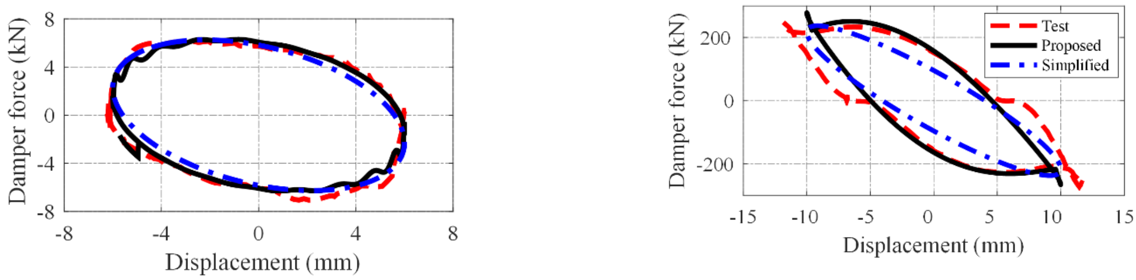

(a) Results of small-scale EIMD (b) Results of full-scale EIMD

Fig. 26 Damper force-displacement plots of the experimental results and simulation results

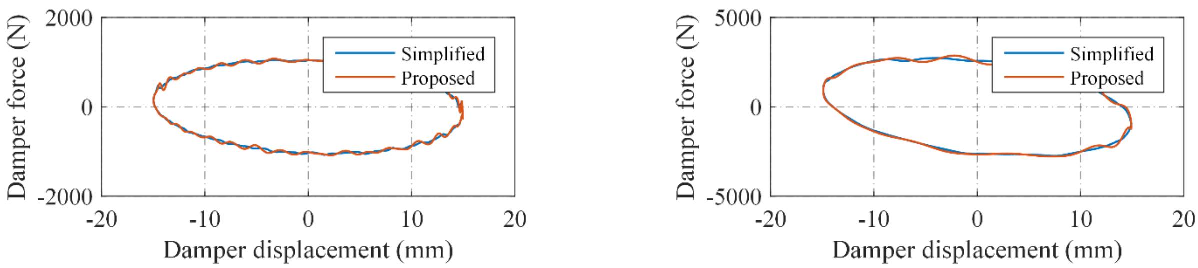

(a) 0.4 Hz (b) 1.0 Hz

Fig. 27 Damper responses comparison, ξ_e=0.1

In Fig. 26, the experimental results are labeled as "Testing", while the simulation results of the proposed model and the previous simplified model are labeled as "Proposed" and "Simplified" respectively. From Fig. 26, it can be observed that: (i) the proposed model can have a better approximation on the damper's performances; (ii) the inaccuracies mentioned in the previous section are largely reduced by the additional electromagnetic element.

However, there are still some differences between the experimental data and simulation results with the proposed model. One of the reasons is due to the simplified behavior of the electromagnetic damper into a viscous element, which can be overcome by using a proper model of the electromagnetic damper in future studies.

4.3 Discussions on the applicability of different damper models

As it is concluded in this section, the proposed analytical model of IMD is better for capturing the damper's self-vibration. Because the IMD device is usually paralleled with an additional energy dissipation device, like a viscous damper, the self-vibration of IMD might be significantly mitigated when the equivalent damping ratio ξ_e is large enough. In that case, the simplified damper model can be used to replace the proposed analytical model. For example, if the ξ_e of the tested damper (Type II) equals to 0.1, the damper responses simulated by the two damper models will be close to each other, as shown in Fig. 27.

Further, Eq. (15) indicates that: the damper force fluctuation caused by the self-vibration of the IMD can be ignored, when the amplitude of x_r is much smaller than that of u_d. Note that, x_i=x_r+u_d, so the transfer function of X_i/U_d can be derived from Eq. (14)

$$G_{X_iU_d}(\omega)=\frac{X_i(\omega)}{U_d(\omega)}=\frac{\omega_e^2}{-\omega^2+2\omega_e\xi_e\omega i+\omega_e^2} \qquad (19)$$

By setting the frequency ratio γ=ω/ω_e, Eq. (19) can be formulated as

$$G_{X_iU_d}(\gamma)=\frac{1}{-\gamma^2+2\xi_e\gamma i+1} \qquad (20)$$

Fig. 28 shows the magnitude plot of transfer function $G_{XiUd}(\gamma)$ for different values of damping ratio ξ_e. It indicates that: only when the frequency ratio γ is close to 1, and the equivalent damping ratio ξ_e is relatively small, the effect of the self-vibration are significant; on the contrary, when γ is small enough (less than about 0.3), or ξ_e is relatively large (larger than about 0.5), the effect of the self-vibration becomes negligible; when γ is large enough (larger than about 1.2), x_i becomes smaller than u_d, and the force-displacement plot will show a positive stiffness, which is in accordance with the results shown in Fig. 9(f).

Table 6 Identified damper parameters of the EIMDs

Damper type	$\overline{m}_e$ (kg)	$\overline{c}_d$ (Ns/m)	k_0 (N/m)	h_d (mm)
Small-scale	6.00×10^3	1.61×10^3	1.03×10^8	0.01
Full-scale	2.20×10^6	2.72×10^6	1.37×10^8	0.40

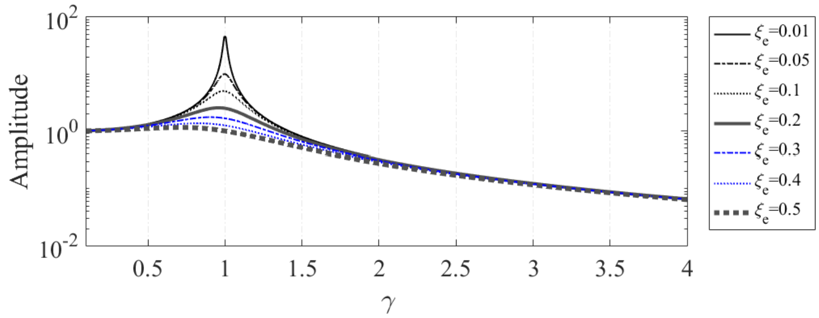

Fig. 28 Magnitude plot of transfer function $G_{XiUd}(\gamma)$for different damping ratios ξ_e

Take the case when γ =1 as an example. If x_i<1.1u_d is treated as the criterion for judging whether the simplified damper model can be used to replace the proposed model, ξ_e should be large than 0.45 according to Eq. (23)

$$\left|G_{X_iU_d}(g=1)\right| = \frac{1}{2x_e} < 1.1 \tag{21}$$

Note that, the above conclusions based on the transfer function of the damper model, are only accurate for the steady-state responses. Specific numbers mentioned above might not be accurate, if the transient responses of the damper are dominant in the practical engineering.

5. Real-time hybrid simulation test for the IMD-cable system

In this section, a real-time hybrid simulation test will be conducted in order to further examine the proposed damper model, and a comparison will be conducted between the results from the experiments and those obtained from the previous study (Lu *et al.* 2017).

Real-time hybrid simulation (RTHS) is an experimental testing method used in structural engineering for performance evaluation of structural systems and its components, which is able to account for rate-of-loading effects on testing (Nakashima *et al.* 1992). This method consists in partitioning a reference structural system, such as a cable-stay bridge with supplemental energy devices, into a physical and numerical substructure. A mathematical model is developed for the numerical substructure, where computers are required to solve for the dynamic response. Meanwhile, the physical substructure is typically chosen to be a critical component of the testing system (e.g., a viscous damper), and is replaced by an experimental test specimen in a laboratory environment. The test specimen is attached to a loading assembly (i.e., actuator), and the experimental responses (displacements and restoring forces) are measured through sensors and data acquisition instruments. Then, the "online" structural testing of the physical specimen is possible, where: (i) the test specimen is loaded with a target displacement obtained from solving the numerical substructure at each time step; and (ii) the measured restoring forces from the test specimen are feedback to the numerical substructure, where the equations of motion are integrated to obtain the next target displacement to be applied to the test specimen. This "hybrid loop" must be performed at very fast speeds, in order to account for rate-of-loading effects. Therefore, the use of dynamically-rated actuators is fundamental to conduct the RTHS testing. In addition, fast computers and algorithms are necessary to execute the RTHS tests in a stable and accurate manner. Also, many cutting-edges improvements have been proposed on this method to make it faster and more reliable, like the new RTHS method based on vector form intrinsic finite element and field programmable gate array (Duan *et al.* 2019a).

The main issue in RTHS testing is the synchronization of target and measured displacements of the test specimen. Since actuators have a dynamic response, a delay could be introduced in the feedback loop, that could affect the accuracy of the RTHS test or even destabilize the loading assembly (Horiuchi *et al.* 1996). Therefore, delay compensation techniques must be incorporated into the experimental design of any RTHS testing.

5.1 Description of test substructures

For this test, the cable-IMD system introduced in Lu *et al.* (2017) is considered as the reference structural system, with same structural parameters. This reference system is partitioned in two substructures as shown in Fig. 29, a numerical substructure consisting of the cable element with distributed mass and intrinsic damping, its supports and transverse loading; meanwhile, the experimental substructure was chosen as the type II inerter. Therefore, a boundary condition at the interface between damper and cable is chosen as a single-degree-of-freedom (SDOF) in RTHS testing, i.e., the stroke of the VIMD damper should be compatible with the transverse displacement of the cable at a distance $\bar{x}_d$ from the left support.

5.2 Test setup and control algorithm

For RTHS test, the same MTS servo-hydraulic actuator system described in Section 3 is considered. In addition, a dSpace DS1103PPC micro-controller with PPC 750GX processor running at 1 GHz, is adopted. The micro-controller will serve the purpose of storing the numerical substructure, conduct real-time numerical computations, and communicate with the MTS servo-controller through

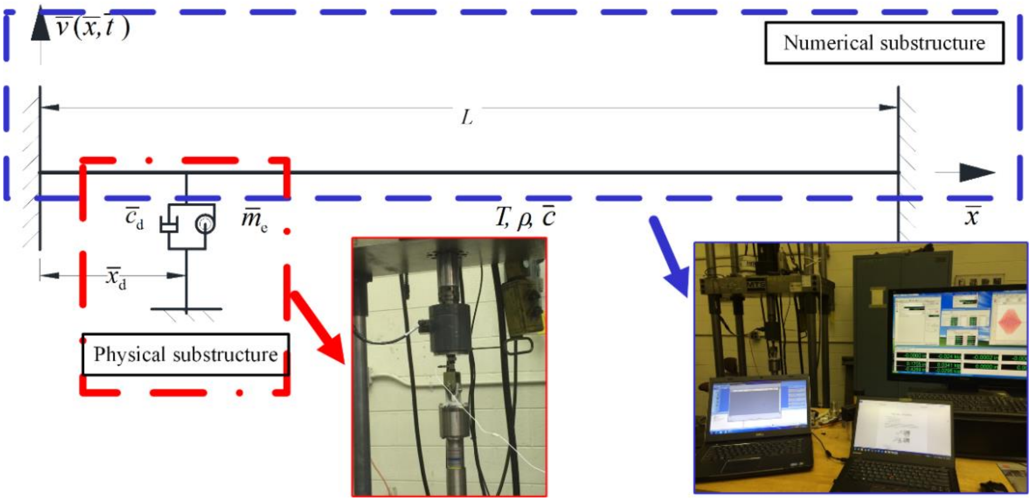

Fig. 29 Numerical and experimental substructures chosen for RTHS test

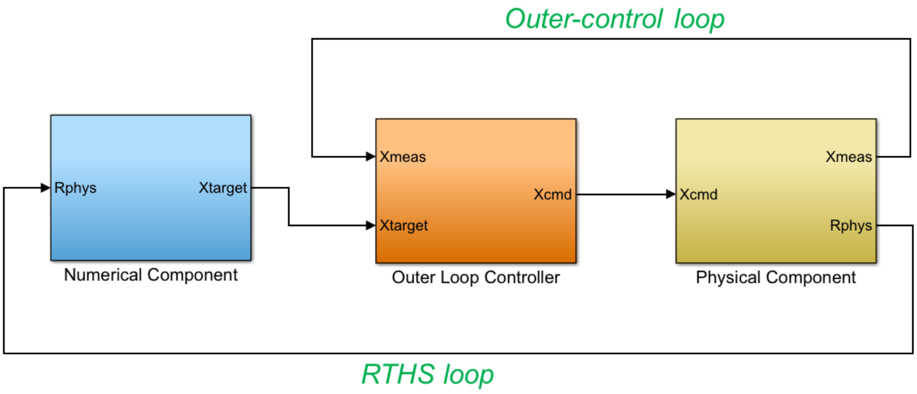

Fig. 30 Block diagram of RTHS algorithmy

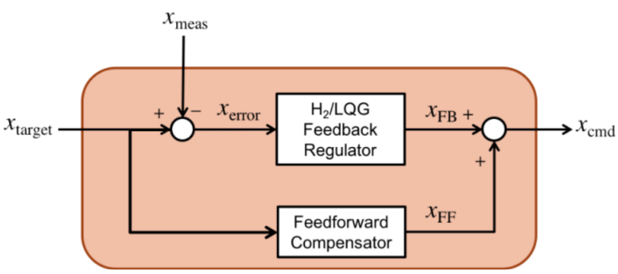

Fig. 31 Outer-control loop algorithm for RTHS testing

16-bit digital-analog converters. In addition, a PCB Signal Conditioner is required for force readings from the PCB piezoelectric load cell.

Henceforth, the RTHS control algorithm is composed of three main subsystems, as shown in Fig. 30: (1) *numerical component*, where the numerical substructure model, external loading, and numerical integration scheme are declared; (2) *outer-loop controller*, where the model-based compensation for servo-hydraulic system dynamics are defined; and (3) *physical component*, where, calibration corrections and digital-analog conversions are conducted to communicate with the external devices in real-time.

For delay compensation, a model-based feedforward-feedback controller is implemented (Phillips and Spencer Jr 2012). The feedforward compensator is used primarily to satisfy the reference tracking (synchronization) objective; meanwhile, the LQG regulator is designed to increase the robustness of the system for any measurement noise or disturbance associated with model uncertainty.

5.3 Results analysis

The results of the distributed sinusoidal load are discussed in this section, while the cable model and load details are similar as those in previous paper (Lu *et al.* 2017).

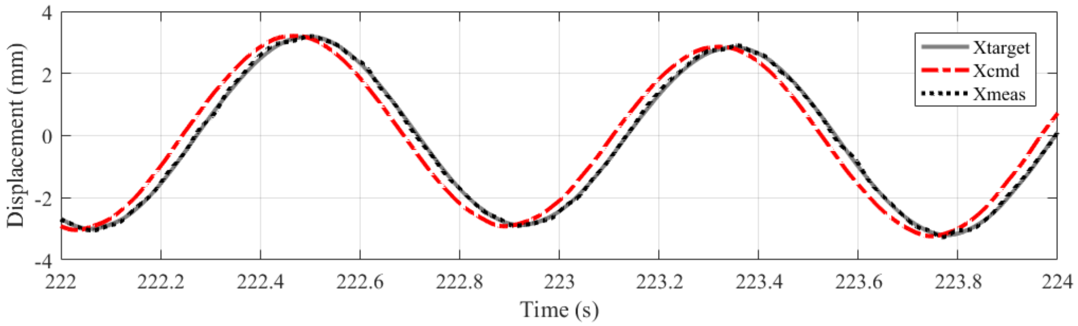

Fig. 32 Comparison of the target, command and measured displacement

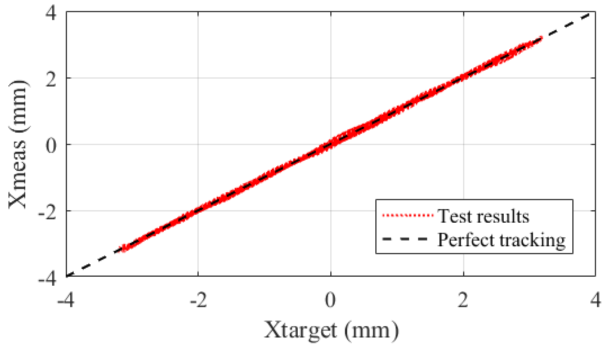

Fig. 33 Synchronization subspace plot of RTHS test results

$$f_n(x,t) = \sin(n\pi x)\cdot\sin(\omega_n t) \tag{22}$$

where n is the mode number. In this paper, n is set to be 3, because damper optimal parameters of mode 3 can be achieved by a relatively small scale factor μ_f (about 59.6) (Lu *et al.* 2017). Other two scale factors μ_i/μ_o are also set at the input/output of the damper, in order to ensure that the damper displacement and force will not exceed any limitations of the testing system.

Note that the optimal damper parameters of the cable-IMD system are given as the normalized equivalent inertial mass m_e and the normalized equivalent damping coefficient $c_d x_d$ in the previous paper (Lu *et al.* 2017), defined as follows

$$x_d = \bar{x}_d / L \qquad m_e = \frac{\bar{m}_e L \omega_0^2}{\pi^2 T} \qquad c_d = \frac{\bar{c}_d L \omega_0}{\pi^2 T} \tag{23}$$

where L is the cable length; T is the tension force of the cable; ω_0 is the fundamental natural frequency of the undamped cable; and x_d is the normalized damper location, preset as 0.02 in this paper. The target normalized optimal damper parameters are m_e=0.53, $c_d x_d$=0.015, and the realized ones in the RTHS are m_e=0.529, $c_d x_d$ =0.0492. To analyze and demonstrate the experimental results, segments of the typical steady-state results are shown as below.

From the results, it can be observed that the model-based controller is able to compensate the actuator dynamics during RTHS test. Fig. 32 shows the time-history plot of the target, command, and measured displacements at the substructures interface, labeled as Xtarget, Xcmd and Xmeas respectively. It is clear that the target and measured signals are almost identical, and that the command signal is always leading the target signal, which was expected because of model-based compensation in RTHS testing. Meanwhile, Fig. 33 shows the synchronization subspace plot, which is a graphical representation of the tracking error in RTHS. This figure shows the measured vs. target displacement data; in the case of perfect tracking, the data should lay in a straight line with slope 1:1. Any deviations from this perfect tracking line can be related experimental errors due to actuator dynamics. Also, it can be seen that the test data follows very well the perfect tracking line; hence, the model-based compensation scheme is successful for conducting RTHS with the IMD device. In terms of performance indices, the root mean square error (RMSE) between the measured and target displacement is around 1.13%, which is considered to be acceptable for this study.

As shown in Fig. 34, the proposed analytical damper model can fit the peak damper forces better than the simplified damper model, and the damper force-displacement plot shows a clearly negative stiffness loop. Meanwhile, the cable displacement responses can still be simulated accurately enough by both damper models. Therefore, the proposed analytical damper model can provide better prediction on the damper behavior, while the simplified damper model is sufficiently accurate for the preliminary simulation of the cable-VIMD system. It also further ensures that the previous conclusion derived with the simplified damper model is correct and reasonable.

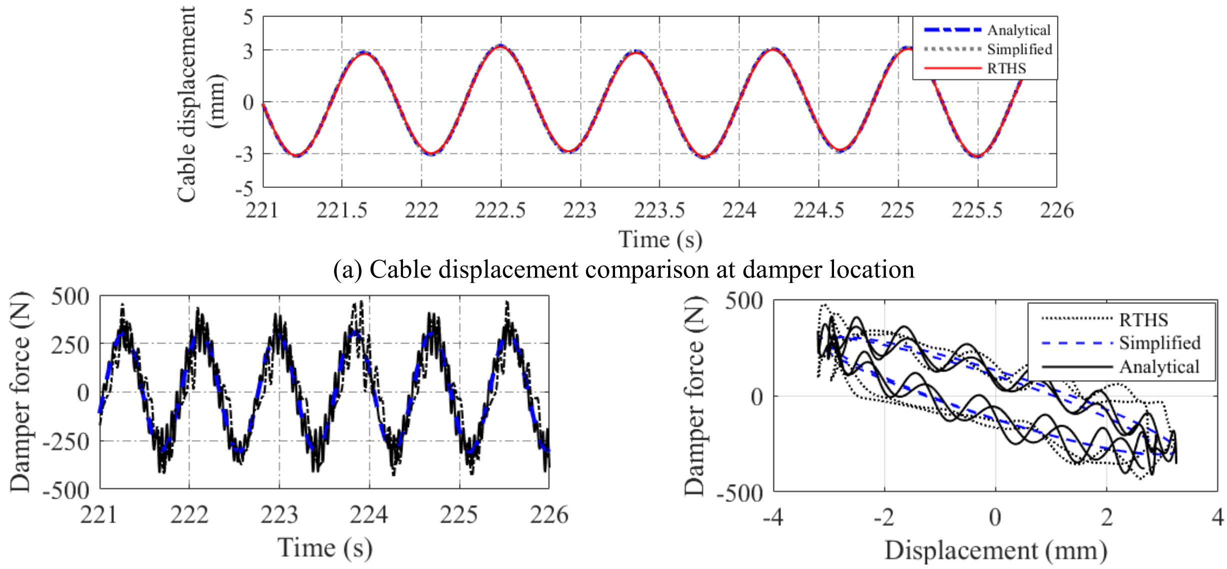

(a) Cable displacement comparison at damper location

(b) Damper force comparison

(c) Damper force-displacement comparison

Fig. 34 Results comparison of RTHS and mock RTHS tests

6. Conclusions

Previous research has shown that the inertial mass damper (IMD) has advantages in the cable vibration control. In this paper, by conducting the damper performance tests, the characteristics of IMD with only the rotary mass part are verified: (i) the inertial mass element can provide clear pseudo-negative stiffness; (ii) the damper force responses have significant high frequency components. Through a detailed analysis, the nonlinearities of the hysteretic loops are related to the damper self-vibration, and the unsmooth input acceleration will lead to abrupt changes of the damper force and excite the high frequency vibration.

Then, an efficient analytical model which can consider the damper's self-vibration with variant stiffness, is introduced. In order to verify the feasibility of this model, parameter identification procedures are conducted based on the experimental results of the tested IMD as well as the data of EIMD from previous studies. By comparing the measured data with the simulation results, the chosen model shows good performance in estimating the behavior of a damper with an inertial mass element.

Finally, the chosen model of the IMD is further validated through a real-time hybrid simulation (RTHS) test, while the accuracy of the simplified damper model is also discussed. It can be concluded that: the introduced model is better when evaluating the damper performances for conceptual design, while the simplified damper model is also feasible for estimating the overall responses of the cable-IMD system.

Acknowledgments

The authors state their sincere gratitude to Sanwa Tekki Corp. for providing the inertial mass damper specimens and enjoy the pleasant discussion with Prof. Sunakoda. The authors also want to thank Mr. Donald Marrow and his colleagues from Newmark Civil Engineering Laboratory at the University of Illinois at Urbana-Champaign (UIUC), for their help during the experiment. Meanwhile, the first author gratefully acknowledges the support of China Scholarship Council (No. 201306260045) and National Natural Science Foundation of China Key Program (No. 51638012) on his research at UIUC. The second author gratefully acknowledges the financial support of CONICYT-Chile through the Becas Chile Scholarship No. 72140204, and Universidad Tecnica Federico Santa Maria (Valparaiso, Chile) through the Faculty Development Program Scholarship No. 208-13. Finally, the fifth author gratefully acknowledges the support of China Scholarship Council on his visit at UIUC and the support of National Natural Science Foundation of China through the Grants 51522811, U1709216, 51178426 and 51478429.

References

Audet, C. and Dennis Jr, J.E. (2002), "Analysis of generalized pattern searches", *SIAM J. Optim.*, **13**(3), 889-903. https://doi.org/10.1137/S1052623400378742.

Cai, C.S., Wu, W.J. and Shi, X.M. (2006), "Cable vibration reduction with a hung-on TMD system. Part I: Theoretical study", *J. Vib. Control*, **12**(7), 801-814. https://doi.org/10.1177/1077546306065857.

Carrie, T.G. (1980), "Guy cable design and damping for vertical axis wind turbines", *SAND80-2669, National Technical Information Service, US Department of Commerce*.

Chen, L., Liu, C., Liu, W., Nie, J., Shen, Y. and Chen, G. (2016a), "Network synthesis and parameter optimization for vehicle suspension with inerter", *Adv. Mech. Eng.*, **9**(1), https://doi.org/10.1177/1687814016684704.

Chen, L., Sun, L.M. and Nagarajaiah, S. (2015a), "Cable with discrete negative stiffness device and viscous damper: passive realization and general characteristics", *Smart Struct. Syst.*,

15(3), 627-643. http://dx.doi.org/10.12989/sss.2015.15.3.627.

Chen, M.Z., Hu, Y., Li, C. and Chen, G. (2016b), "Application of semi-active inerter in semi-active suspensions via force tracking", *J. Vib. Acoust.*, **138**(4), 041014. doi: 10.1115/1.4033357.

Chen, M.Z., Papageorgiou, C., Scheibe, F., Wang, F.C. and Smith, M.C. (2009), "The missing mechanical circuit element", *IEEE Circuits Syst. Magazine*, **9**(1). doi: 10.1109/MCAS.2008.931738

Chen, Z.Q., Huang, Z.W. and Hua, X.G. (2015b), "Inerter-damper-spring passive vibraiton control: its system reliazation with eddy-current mass dampers", *Proceedings of the 14th World Conference on Seismic Isolation, Energy dissipation and Active Control of Structures*, San Diego, USA.

Chen, Z.Q., Wang, X.Y., Ko, J.M., Ni, Y.Q., Spencer, B.F. Jr., Yang, G. and Hu, J.H. (2004), "MR damping system for mitigating wind-rain induced vibration on Dongting Lake Cable-Stayed Bridge", *Wind Struct.*, **7**(5), 293-304. http://dx.doi.org/10.12989/was.2004.7.5.293.

Duan, Y., Tao, J., Zhang, H., Wang, S. and Yun, C. (2019a), "Real-time hybrid simulation based on vector form intrinsic finite element and field programmable gate array", *Struct. Control Health Monit.*, **26**(1), e2277. https://doi.org/10.1002/stc.2277

Duan, Y.F., Ni, Y.Q. and Ko, J.M. (2005), "State-derivative feedback control of cable vibration using semiactive magnetorheological dampers", *Comput.-Aided Civil Infrastruct. Eng.*, **20**(6), 431-449. https://doi.org/10.1111/j.1467-8667.2005.00396.x.

Duan, Y.F., Ni, Y.Q. and Ko, J.M. (2006), "Cable vibration control using magnetorheological dampers", *J. Intel. Mat. Syst. Struct.*, **17**(4), 321-325.

Duan, Y.F., Ni, Y.Q., Ko, J.M. and Dong, S.L. (2007), "Design of MR dampers for open-loop vibration control of stay cables on cable supported structures", *Spatial Struct.*, **13**(2), 58-64.

Duan, Y.F., Ni, Y.Q., Zhang, H.M., Spencer, B.F. Jr. and Ko, J.M. (2019b), "Design formulas for vibration control of sagged cables using passive MR dampers", *Smart Struct. Syst.*, Accepted.

Duan, Y.F., Ni, Y.Q., Zhang, H.M., Spencer, B.F. Jr. and Ko, J.M. (2019c), "Design formulas for vibration control of taut cables using passive MR dampers", *Smart Struct. Syst.*, Accepted.

Firestone, F.A. (1933), "A new analogy between mechanical and electrical systems", *J. Acoust. Soc. Am.*, **4**(3), 249-267. https://doi.org/10.1121/1.1915605.

Fujino, Y. and Hoang, N. (2008), "Design formulas for damping of a stay cable with a damper", *J. Struct. Eng.*, **134**(2), 269-278. https://doi.org/10.1061/(ASCE)0733-9445(2008)134:2(269).

Giaralis, A. and Marian, L. (2016), "Use of inerter devices for weight reduction of tuned mass-dampers for seismic protection of multi-story building: the Tuned Mass-Damper-Interter (TMDI)", *SPIE Smart Structures and Materials+ Nondestructive Evaluation and Health Monitoring*.

Giaralis, A. and Petrini, F. (2017), "Wind-induced vibration mitigation in tall buildings using the tuned mass-damper-inerter (TMDI)", *J. Struct. Eng.*, **143**(9), https://doi.org/10.1061/(ASCE)ST.1943-541X.0001863

Gonzalez-Buelga, A., Lazar, I.F., Jiang, J.Z., Neild, S.A. and Inman, D.J. (2017), "Assessing the effect of nonlinearities on the performance of a tuned inerter damper", *Struct. Control Health Monit.*, **24**(3), https://doi.org/10.1002/stc.1879.

Gonzalez-Buelga, A., Clare, L., Neild, S., Burrow, S. and Inman, D. (2015), "An electromagnetic vibration absorber with harvesting and tuning capabilities", *Struct. Control Health Monit.*, **22**(11), 1359-1372. https://doi.org/10.1002/stc.1748.

Gu, M., Xiang, H.F. and Chen, A.R. (1994), "A practical method of passive TMD for suppressing wind-induced vertical buffeting of long-span cable-stayed bridges and its application", *J. Wind Eng. Ind. Aerod.*, **51**(2), 203-213. https://doi.org/10.1016/0167-6105(94)90004-3.

Høgsberg, J. and Krenk, S. (2017), "Calibration of piezoelectric RL shunts with explicit residual mode correction", *J. Sound Vib.*, **386**, 65-81. https://doi.org/10.1016/j.jsv.2016.08.028.

Hessabi, R.M. and Mercan, O. (2016), "Investigations of the application of gyro-mass dampers with various types of supplemental dampers for vibration control of building structures", *Eng. Struct.*, **126**, 174-186. https://doi.org/10.1016/j.engstruct.2016.07.045.

Horiuchi, T., Nakagawa, M., Sugano, M. and Konno, T. (1996), "Development of a real-time hybrid experimental system with actuator delay compensation", *Proceedings of the 11th World Conf. Earthquake Engineering*.

Hwang, J.S., Kim, J. and Kim, Y.M. (2007), "Rotational inertia dampers with toggle bracing for vibration control of a building structure", *Eng. Struct.*, **29**(6), 1201-1208. https://doi.org/10.1016/j.engstruct.2006.08.005.

Hjgsberg, J. and Krenk, S. (2016), "Accurate calibration of RL shunts for piezoelectric vibration damping of flexible structures", *Proceedings of the 27th International Conference on Adaptive Structures and Technologies (icast 2016)*.

Ikago, K., Saito, K. and Inoue, N. (2012a), "Seismic control of single-degree-of-freedom structure using tuned viscous mass damper", *Earthq. Eng. Struct. D.*, **41**(3), 453-474. https://doi.org/10.1002/eqe.1138.

Ikago, K., Sugimura, Y., Saito, K. and Inoue, N. (2012b), "Modal response characteristics of a multiple-degree-of-freedom structure incorporated with tuned viscous mass dampers", *J. Asian Architect. Build. Eng.*, **11**(2), 375-382. https://doi.org/10.3130/jaabe.11.375.

Kawaguchi, O., Kanoh, T., Akino, K., Kato, M. and Sunakoda, K. (1991), "Research and development of seismic restraint snubbers,(1)", *Nippon Genshiryoku Gakkai-Shi*, **33**(1), 76-89.

Kawamata, S. (1989), *Liquid type mass damper with elongated discharge tube*, Google Patents

Kelly, J. (1997), "Experimental study of mechanical pipe snubber seismic behavior".

Kovacs, I. (1982), "Zur frage der seilschwingungen und der seildämpfung", *Bautechnik*, **59**(10).

Krenk, S. and Høgsberg, J.R. (2005), "Damping of cables by a transverse force", *J. Eng. Mech.*, **131**(4), 340-348. https://doi.org/10.1061/(ASCE)0733-9399(2005)131:4(340).

Krenk, S. and Nielsen, S.R. (2002), "Vibrations of a shallow cable with a viscous damper", *Proceedings of the Royal Society of London A: Mathematical, Physical and Engineering Sciences*.

Lazar, I., Neild, S. and Wagg, D. (2014a), "Inerter-based vibration suppression systems for laterally and base-excited structures", *Proceedings of EURODYN 2014*.

Lazar, I., Neild, S. and Wagg, D. (2014b), "Using an inerter-based device for structural vibration suppression", *Earthq. Eng. Struct. D.*, **43**(8), 1129-1147. https://doi.org/10.1002/eqe.2390.

Lazar, I., Neild, S. and Wagg, D. (2016), "Vibration suppression of cables using tuned inerter dampers", *Eng. Struct.*, **122**, 62-71. https://doi.org/10.1016/j.engstruct.2016.04.017.

Lazar, I.F., Neild, S.A. and Wagg, D.J. (2014c), *Design and performance analysis of inerter-based vibration control systems*, Dynamics of Civil Structures, Volume 4, Springer

Lazar, I.F., Neild, S.A. and Wagg, D.J. (2015), *Performance analysis of cables with attached tuned-inerter-dampers*, Dynamics of Civil Structures, Volume 2, Springer

Liu, Y., Chen, M.Z. and Tian, Y. (2015), "Nonlinearities in landing gear model incorporating inerter", *Information and Automation, 2015 IEEE International Conference on*.

Lu, L., Duan, Y.F., Spencer, B.F. Jr., Lu, X.L. and Zhou, Y. (2017), "Inertial mass damper for mitigating cable vibration", *Struct. Control Health Monit.*, **24**(10), https://doi.org/10.1002/stc.1986.

Luo, J., Jiang, J.Z. and Macdonald, J.H. (2016), "Damping

Performance of Taut Cables with Passive Absorbers Incorporating Inerters", *J. Phys.: Conference Series*.

Main, J. and Jones, N. (2002a), "Free vibrations of taut cable with attached damper. I: Linear viscous damper", *J. Eng. Mech.*, **128**(10), 1062-1071. https://doi.org/10.1061/(ASCE)0733-9399(2002)128:10(1062).

Main, J. and Jones, N. (2002b), "Free vibrations of taut cable with attached damper. II: Nonlinear damper", *J. Eng. Mech.*, **128**(10), 1072-1081. https://doi.org/10.1061/(ASCE)0733-9399(2002)128:10(1072).

Makris, N. and Kampas, G. (2016), "Seismic Protection of Structures with Supplemental Rotational Inertia", *J. Eng. Mech.*, **142**(11), 04016089. https://doi.org/10.1061/(ASCE)EM.1943-7889.0001152.

Marian, L. and Giaralis, A. (2013), "Optimal design of inerter devices combined with TMDs for vibration control of buildings exposed to stochastic seismic excitations", *Proceedings of the 11th International Conference on Structural Safety and Reliability for Integrating Structural Analysis, Risk and Reliability (ICOSSAR 2013)*.

Marian, L. and Giaralis, A. (2014), "Optimal design of a novel tuned mass-damper–inerter (TMDI) passive vibration control configuration for stochastically support-excited structural systems", *Probabilist. Eng. Mech.*, **38**, 156-164. https://doi.org/10.1016/j.probengmech.2014.03.007.

Nakamura, Y., Fukukita, A., Tamura, K., Yamazaki, I., Matsuoka, T., Hiramoto, K. and Sunakoda, K. (2014), "Seismic response control using electromagnetic inertial mass dampers", *Earthq. Eng. Struct. D.*, **43**(4), 507-527. https://doi.org/10.1002/eqe.2355.

Nakamura, Y., Hanzawa, T. and Isoda, K. (2013), "Performance-based placement design of tuned inertial mass dampers", *Proceedings of the 13th World Conference on Seismic Isolation*, Sendai, Japan.

Nakamura, Y., Watanabe, H. and Kawamata, S. (1988), "Seismic response control of structures by accelerated liquid mass damper", *Proceedings of the 9th World Conference on Earthquake Engineering*.

Nakashima, M., Kato, H. and Takaoka, E. (1992), "Development of real-time pseudo dynamic testing", *Earthq. Eng. Struct. D.*, **21**(1), 79-92. https://doi.org/10.1002/eqe.4290210106.

Ohtake, T., Sunakoda, K. and Matsuoka, T. (2006), "Study on vibration control device using power generator", *Proceedings of the ASME 2006 Pressure Vessels and Piping/ICPVT-11 Conference*.

Okamoto, M., Tsuyuki, Y. and Matsui, K. (2017), "Development and application example of rotational inertia mass damper", *Proceedings of the 16th World Conference on Earthquake Engineering*, Santiago, Chile.

Or, S.W., Duan, Y.F., Ni, Y.Q., Chen, Z.H. and Lam, K.H. (2008), "Development of magnetorheological dampers with embedded piezoelectric force sensors for structural vibration control", *J. Intel. Mat. Syst. Str.*, **19**(11), 1327-1338. https://doi.org/10.1177/1045389X07085673.

Pacheco, B.M., Fujino, Y. and Sulekh, A. (1993), "Estimation curve for modal damping in stay cables with viscous damper", *J. Struct. Eng.*, **119**(6), 1961-1979. https://doi.org/10.1061/(ASCE)0733-9445(1993)119:6(1961).

Papageorgiou, C., Houghton, N.E. and Smith, M.C. (2009), "Experimental testing and analysis of inerter devices", *J. Dyn. Syst. Meas. Control*, **131**(1), 011001. doi:10.1115/1.3023120.

Papageorgiou, C. and Smith, M.C. (2005), "Laboratory experimental testing of inerters", *Proceedings of the Decision and Control, 2005 and 2005 European Control Conference. CDC-ECC'05. 44th IEEE Conference on*.

Phillips, B.M. and Spencer, B.F. Jr. (2012), "Model-based feedforward-feedback actuator control for real-time hybrid simulation", *J. Struct. Eng.*, **139**(7), 1205-1214. https://doi.org/10.1061/(ASCE)ST.1943-541X.0000606.

Pietrosanti, D., De Angelis, M. and Basili, M. (2017), "Optimal design and performance evaluation of systems with Tuned Mass Damper Inerter (TMDI)", *Earthq. Eng. Struct. D.*, **46**(8), 1367-1388. https://doi.org/10.1002/eqe.2861.

Saito, K., Yogo, K., Sugimura, Y., Nakaminami, S. and Park, K. (2004), "Application of rotary inertia to displacement reduction for vibration control system", *Proceedings of the 13th World Conference on Earthquake Engineering*.

Saitoh, M. (2012), "On the performance of gyro-mass devices for displacement mitigation in base isolation systems", *Struct. Control Health Monit.*, **19**(2), 246-259. https://doi.org/10.1002/stc.419.

Severud, L. and Summers, G. (1980), *Design considerations for mechanical snubbers*, Hanford Engineering Development Lab., Richland, WA (USA)

Shen, Y., Chen, L., Liu, Y. and Zhang, X. (2016a), "Modeling and optimization of vehicle suspension employing a nonlinear fluid inerter", *J. Shock Vib.*, **2016**. http://dx.doi.org/10.1155/2016/2623017.

Shen, Y., Chen, L., Yang, X., Shi, D. and Yang, J. (2016b), "Improved design of dynamic vibration absorber by using the inerter and its application in vehicle suspension", *J. Sound Vib.*, **361**, 148-158. https://doi.org/10.1016/j.jsv.2015.06.045.

Smith, M.C. (2002), "Synthesis of mechanical networks: The inerter", *IEEE T. Autom. Control*, **47**(10), 1648-1662. doi: 10.1109/TAC.2002.803532.

Sun, X.Q., Chen, L., Wang, S.H., Zhang, X.L. and Yang, X.F. (2016), "Performance investigation of vehicle suspension system with nonlinear ball-screw inerter", *Int. J. Autom. Techn.*, **17**(3), 399-408.

Swift, S., Smith, M.C., Glover, A., Papageorgiou, C., Gartner, B. and Houghton, N.E. (2013), "Design and modelling of a fluid inerter", *Int. J. Control*, **86**(11), 2035-2051. https://doi.org/10.1080/00207179.2013.842263

Tabatabai, H. and Mehrabi, A.B. (2000), "Design of mechanical viscous dampers for stay cables", *J. Bridge Eng.*, **5**(2), 114-123. https://doi.org/10.1061/(ASCE)1084-0702(2000)5:2(114).

Wang, F.C., Chen, Y.C. and Lee, C.H. (2016), "Design and optimization of inerter layouts for a multi-layers building model", *Proceedings of the 2016 55th Annual Conference of the Society of Instrument and Control Engineers of Japan (SICE)*.

Wang, F.C., Hong, M.F. and Lin, T.C. (2011), "Designing and testing a hydraulic inerter", *Proceedings of the Institution of Mechanical Engineers, Part C: Journal of Mechanical Engineering Science*, **225**(1), 66-72.

Wang, F.C. and Su, W.J. (2008a), "Inerter nonlinearities and the impact on suspension control", *Proceedings of the American Control Conference, 2008*.

Wang, F. and Su, W. (2008b), "Impact of inerter nonlinearities on vehicle suspension control", *Vehicle Syst. Dyn.*, **46**(7), 575-595. https://doi.org/10.1080/00423110701519031.

Wang, X.Y., Ni, Y.Q., Ko, J.M. and Chen, Z.Q. (2005), "Optimal design of viscous dampers for multi-mode vibration control of bridge cables", *Eng. Struct.*, **27**(5), 792-800. https://doi.org/10.1016/j.engstruct.2004.12.013.

Watanabe, Y., Ikago, K., Inoue, N., Kida, H., Nakaminami, S., Tanaka, H., Sugimura, Y. and Saito, K. (2012), "Full-scale dynamic tests and analytical verification of a force-restricted tuned viscous mass damper", *Proceedings of the 15th World Conference on Earthquake Engineering*, Lisbon, Portugal.

Watson, S.C. and Stafford, D.G. (1988), "Cables in trouble", *Civil Eng. - ASCE*, **58**(4), 38-41.

Weber, F., Høgsberg, J. and Krenk, S. (2010), "Optimal tuning of amplitude proportional Coulomb friction damper for maximum cable damping", *J. Struct. Eng.*, **136**(2), 123-134.

https://doi.org/10.1061/(ASCE)0733-9445(2010)136:2(123).

Wen, Y., Chen, Z. and Hua, X. (2016), "Design and evaluation of tuned inerter-based dampers for the seismic control of MDOF structures", *J. Struct. Eng.*, 04016207.

Wu, W.J. and Cai, C.S. (2006), "Cable vibration reduction with a hung-on TMD system, Part II: parametric study", *J. Vib. Control*, **12**(8), 881-899. https://doi.org/10.1177/1077546306065858.

Xu, Y.L. and Yu, Z. (1998), "Mitigation of three-dimensional vibration of inclined sag cable using disrete oil dampers — II. Application", *J. Sound Vib.*, **214**(4), 675-693. https://doi.org/10.1006/jsvi.1998.1630.

Yamaguchi, H. and Fujino, Y. (1998), "Stayed cable dynamics and its vibration control", *Bridge Aerod.*, 235-254.

Yu, Z. and Xu, Y.L. (1998), "Mitigation of three-dimensional vibration of inclined sag cable using discrete oil dampers — I. Formulation", *J. Sound Vib.*, **214**(4), 659-673.

Zhang, S.Y., Jiang, J.Z. and Neild, S. (2016), "Passive vibration suppression using inerters for a multi-storey building structure", *Journal of Physics: Conference Series*.

Zhang, S.Y., Jiang, J.Z. and Neild, S. (2017), "Optimal configurations for a linear vibration suppression device in a multi-storey building", *Struct. Control Health Monit.*, **24**(3), https://doi.org/10.1002/stc.1887.

Zhou, H.J., Sun, L.M. and Xing, F. (2014), "Damping of full-scale stay cable with viscous damper: experiment and analysis", *Adv. Struct. Eng.*, **17**(2), 265-274. https://doi.org/10.1260/1369-4332.17.2.265.